Cell Reports
Medicine

Article

Interferon-γ-stimulated antigen-presenting cancer-associated fibroblasts hinder neoadjuvant chemoimmunotherapy efficacy in lung cancer

Graphical abstract

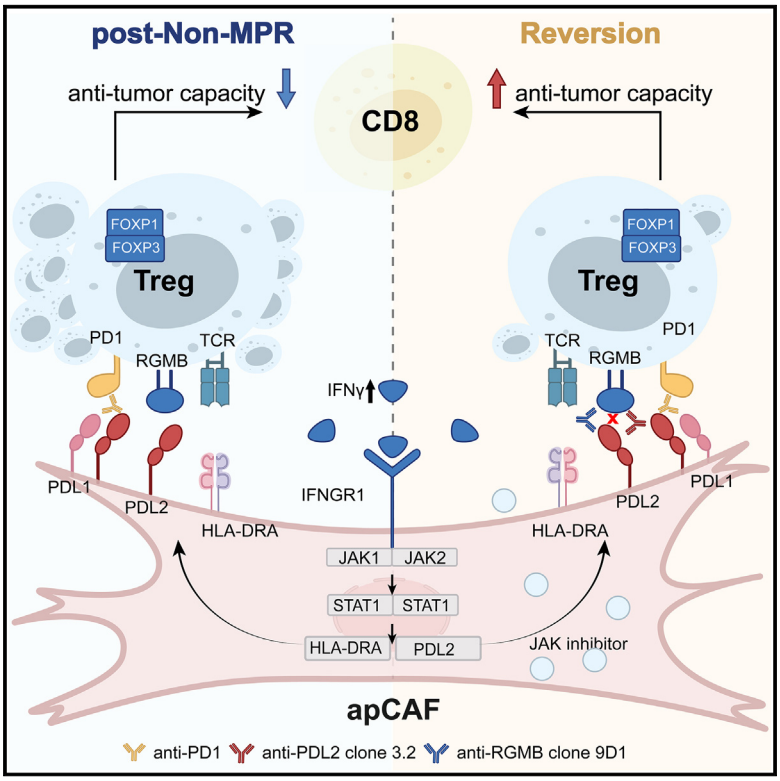

Highlights

- apCAFs are associated with unfavorable outcomes in NSCLC patients receiving NCIT
- apCAFs' expansion is triggered by IFN-γ via the JAK1/2-STAT1 pathway
- apCAFs promote the formation of FOXP1^{+}Tregs through the PD-L2-RGMB axis
- Targeting apCAFs by the blockade of the PD-L2-RGMB axis improves immunotherapy efficacy

Authors

Zhengqi Cao, Zhouwenli Meng, Jian Li, ..., Lixuan Chen, Shun Lu, Ziming Li

Correspondence

shunlu@sjtu.edu.cn (S.L.),
liziming1980@shsmu.edu.cn (Z.L.)

In brief

Cao et al. reveal that antigen-presenting cancer-associated fibroblasts (apCAFs) hinder NCIT effectiveness in NSCLC. IFN-γ induces apCAF expansion, which promotes FOXP1^{+}Treg formation through the PD-L2-RGMB axis. Targeting this pathway enhances immunotherapy outcomes, offering a potential therapeutic strategy.

Cao et al., 2025, Cell Reports Medicine 6, 102017
March 18, 2025
https://doi.org/10.1016/j.xcrm.2025.102017

CellPress

Cell Reports Medicine

CellPress
OPEN ACCESS

Article

Interferon-γ-stimulated antigen-presenting cancer-associated fibroblasts hinder neoadjuvant chemoimmunotherapy efficacy in lung cancer

Zhengqi Cao,[1,2] Zhouwenli Meng,[1,2] Jian Li,[1,2] Yu Tian,[1] Li Lu,[1] Anni Wang,[1] Jia Huang,[1] Jingze Wang,[1] Jing Sun,[1] Lixuan Chen,[1] Shun Lu,[1,*] and Ziming Li[1,3,*]

[1]Shanghai Lung Cancer Center, Shanghai Chest Hospital, Shanghai Jiaotong University, School of Medicine, Shanghai 200030, P.R. China
[2]These authors contributed equally
[3]Lead contact
*Correspondence: shunlu@sjtu.edu.cn (S.L.), liziming1980@shsmu.edu.cn (Z.L.)
https://doi.org/10.1016/j.xcrm.2025.102017

SUMMARY

Conventional neoadjuvant chemotherapy provides limited benefit for patients with resectable non-small cell lung cancer (NSCLC). Recently, neoadjuvant chemoimmunotherapy (NCIT) has transformed the perioperative management of NSCLC by priming systemic anti-tumor immunity before surgery, yet it remains ineffective for at least 50% of patients. Through single-cell sequencing analysis of our NCIT cohort, we identify that antigen-presenting cancer-associated fibroblasts (apCAFs) can impede the efficacy of NCIT. Using a custom cancer-associated fibroblast biobank, we uncover that interferon (IFN)-γ stimulates apCAF expansion via the JAK1/2-STAT1-IFI6/27 pathway. Mechanistically, apCAFs significantly contribute to PD-L2 expression in the tumor microenvironment (TME), triggering the accumulation of FOXP1^{+}regulatory T cells (Tregs) through the PD-L2-RGMB axis. Reprogramming apCAFs by inhibiting the IFN-γ pathway or blocking the PD-L2-RGMB axis substantially mitigates apCAFs-mediated FOXP1^{+}Tregs' expansion. In summary, we reveal the role of apCAFs in compromising NCIT efficacy and propose applications for anti-PD-L2/RGMB regimens to synergize with anti-PD1 therapies by targeting apCAFs.

INTRODUCTION

Neoadjuvant therapy has revolutionized perioperative regimens for cancer patients.[1–3] One notable example is neoadjuvant chemoimmunotherapy (NCIT), which was associated with significantly greater event-free survival than neoadjuvant chemotherapy (NCT) alone.[3] The efficacy of neoadjuvant therapy is primarily assessed by the major pathological response (MPR) rate, defined as less than 10% residual viable tumor in the resected specimen.[4] Non-small cell lung cancer (NSCLC) was the first cancer type reported to benefit from neoadjuvant immune checkpoint inhibitors (neo-ICIs).[5] Meanwhile, NCIT has become the dominant therapeutic approach in the neoadjuvant setting, extending its use in clinical practice due to its promising clinical response rates compared to either NCT[6] or neo-ICIs alone.[7] The NADIM-2 phase 2 randomized trial highlighted that the pathologically complete regression (pCR) rate improved to 37% in the nivolumab plus chemotherapy group compared to 7% with chemotherapy alone.[6] Furthermore, the KEYNOTE-671[6] and AEGEAN[8] trials indicated that neoadjuvant anti-PD1/L1 regimens plus chemotherapy confer greater benefits compared to NCT alone.[9,10] Despite these promising results, the non-MPR rate remains high, reaching approximately 60% in the CheckMate 816 trial.[11] Furthermore, the LCMC3 trial reported a higher non-MPR rate of 80%, with 9% experiencing progressive disease (PD). However, the specific mechanisms responsible for non-MPR remain largely unknown.[12] This clinical evidence underscores the need to develop new strategies to overcome resistance to NCIT.

Cancer-associated fibroblasts (CAFs) are the predominant type of stromal cells in the tumor microenvironment (TME).[13] CAFs can induce immunosuppressive effects by interacting with T cells[14] and tumor-associated macrophages,[15] among others. Numerous studies have demonstrated their tumor-promoting behaviors. Recently, a few studies exploring their role in immunotherapy resistance have emerged. Liang et al. unveiled that autophagy-enhanced CAFs could compromise immunotherapy by up-regulating PD-L1.[14] Similarly, Lin et al. identified biglycan-secreting CAFs as a barrier to anti-PD1 efficacy.[16] However, the role of specific CAF subtypes in inducing anti-PD1 resistance in NSCLC, particularly in the context of NCIT, remains unexplored. In this study, using single-cell RNA sequencing (scRNA-seq), digital spatial profiling (DSP) spatial sequencing, and bulk RNA sequencing (RNA-seq) of patients' tumor samples during NCIT, we identified that antigen-presenting cancer-associated fibroblasts (apCAFs) are associated with NCIT non-MPR in NSCLC patients.

apCAFs are a newly identified CAF subcluster characterized by major histocompatibility complex (MHC)II expression.[17] Brekken et al. reported apCAFs in the pancreatic ductal

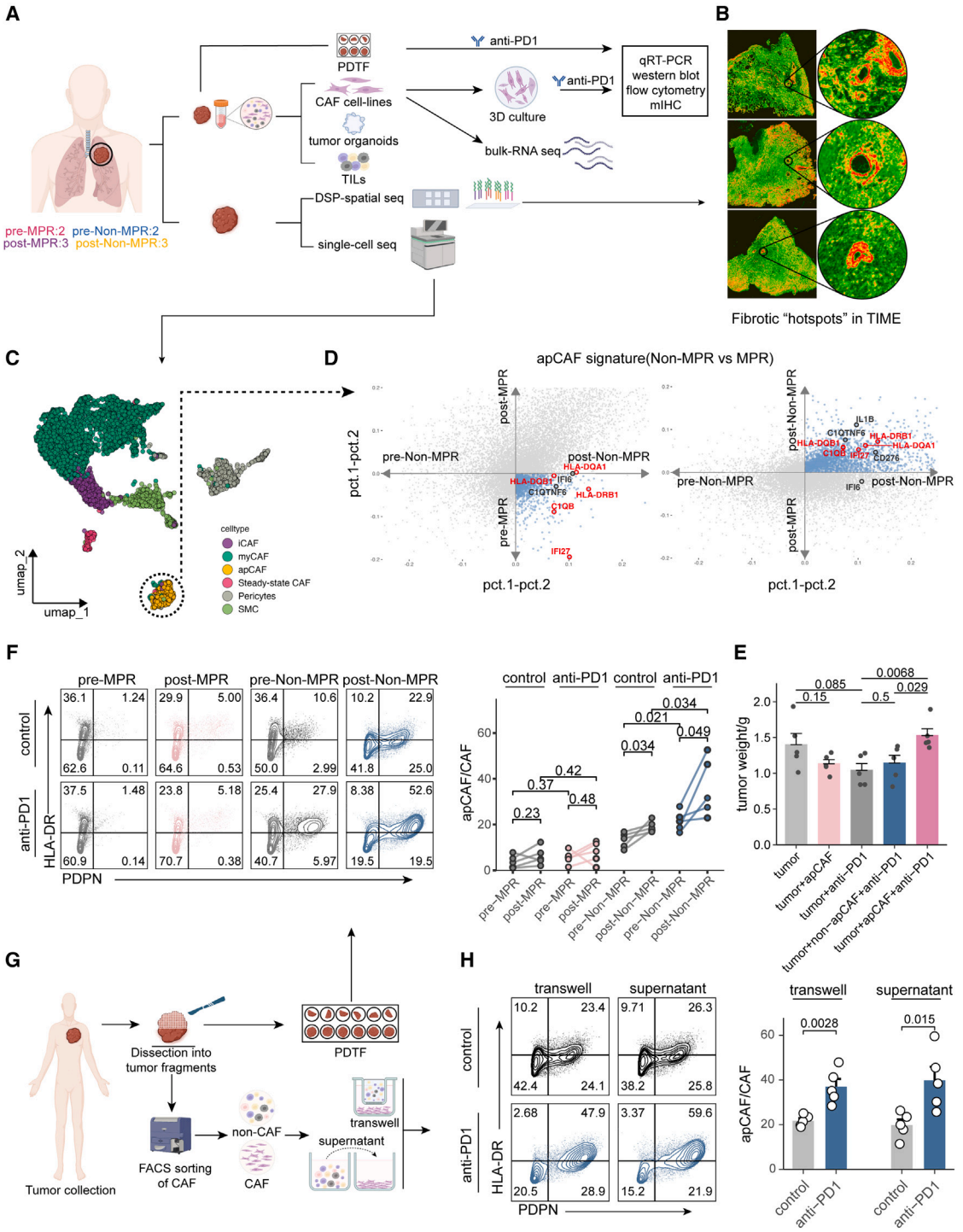

Figure 1. apCAFs accumulated in TME of post-non-MPR

(A) Experimental design and the patient cohort. The respective experimental details referred to here are in the STAR Methods.

(B) Three representative immunohistochemistry (IHC) pictures of fibrotic "hotspots" in non-small cell lung cancer (NSCLC) TME sequenced by DSP spatial sequencing.

(C) Uniform manifold approximation and projection (UMAP) plot of 6,987 CAF cells colored by clusters in our NCIT cohort. "apCAF" is encircled by a dashed line.

(D) Scatterplot showing gene expression change for post-non-MPR versus pre-non-MPR (x axis) against the post-MPR versus pre-MPR (y axis, left) or post-non-MPR versus post-MPR (y axis, right) in all CAFs. Genes significantly upregulated in post-non-MPR versus pre-non-MPR while downregulated in post-MPR versus

(legend continued on next page)

adenocarcinoma (PDAC) TME and confirmed that apCAFs could induce regulatory T cell (Treg) expansion in *ex vivo* assays, although the exact mechanism remained unclear.[17] Jiang et al. further reported that apCAF accumulation also depended on the interleukin (IL)-1-IL-1R2 signaling pathway in Tregs.[18] However, their specific function in NSCLC, particularly in the context of NCIT, was largely unknown. Through our previously developed cell-communication analysis pipeline[19] and a 3D *ex vivo* co-culture platform,[20] we discovered that the expansion of apCAFs, which relied upon anti-PD1, could promote FOXP1$^+$ Treg accumulation via the PD-L2-repulsive guidance molecule b (RGMB) axis, thereby dampening anti-PD1 efficacy in NSCLC, in turn. Mechanistically, we discovered that anti-PD1 could augment apCAF expansion dependent on interferon (IFN)-γ, which stimulated the JAK1/2-STAT1-IFI6/27 axis, ultimately leading to the upregulation of MHCII and PD-L2.

PD-L2, another PD1 ligand, showed limited efficacy with anti-PD-L2 therapies for a long time.[21] Sharpe et al. recently found RGMB as a new key PD-L2 partner, and combining anti-RGMB with anti-PD1 may overcome microbiome-mediated immunotherapy resistance.[22] However, the specific cell cluster responsible for RGMB expression remained unknown. In our study, we identified Tregs as the major contributors to RGMB expression in the TME. Additionally, we found that apCAFs were the primary source of PD-L2 expression. Utilizing murine tumor models and organoid platforms, we confirmed that, in apCAF-enriched lung tumors, targeting the PD-L2-RGMB axis could significantly overcome anti-PD1 resistance. This finding not only provides additional therapeutic options for addressing NCIT resistance but also opens potential application opportunities for anti-PD-L2 regimens in clinical settings.

RESULTS

Antigen-presenting CAFs specifically enriched in the TME of post-non-MPR

The TME is a complex ecosystem composed of tumor, immune, and stromal cells. Recently, Ye et al. identified fibroblasts as the dominant stromal cells subtype.[23] Moreover, several studies have demonstrated the influence of fibroblasts on immunotherapy.[16,24] Coincidentally, we uncovered that higher expression of the CAF signature was significantly correlated with worse progression-free survival in a public NSCLC cohort treated with immune checkpoint inhibitors (ICIs) as well[25] (Figure S1A). To deeply explore fibroblasts in NCIT, we conducted scRNA-seq on tumor specimens from 10 NSCLC patients and DSP spatial sequencing on specimens from 6 patients, either before or after NCIT (Figure 1A). Smooth-muscle actin (SMA) was a typical marker of CAFs, and we therefore selected SMA$^+$ cells within the TME for DSP spatial sequencing (Figure 1B). To comprehensively analyze the phenotypic changes within different TME components during NCIT treatments, we collected, sorted, and cultured primary CAF cell lines (37 patients), tumor-infiltrating lymphocytes (TILs), and organoids (11 patients). CAF cell lines were cultured in a 3D manner in the non-immunogenic hydrogel that was developed by us,[19,20] followed by various readouts (Figure 1A).

During the scRNA-seq analysis, we used COL1A1 and COL3A1 as exclusive markers for CAFs and excluded contamination by other cell types using digital flow cytometry sorting (fluorescence-activated cell sorting [FACS]) (Figures S1B–S1E). In total, we identified 6,987 CAF cells and categorized them into 6 distinct subtypes (Figure 1C). Differential gene (DEG) analysis revealed unique expression patterns across these subtypes (Figures S1F and S1G). To investigate the potential changes within different CAF subtypes during NCIT, we conducted DEG analysis systematically in all CAFs, comparing specimens before (pre-non-MPR and pre-MPR) and after NCIT (post-non-MPR and post-MPR).

Interestingly, we found that the signature genes of apCAFs[17] were significantly upregulated in post-non-MPR samples compared to both pre-non-MPR and post-MPR samples (Figure 1D). Conversely, these genes were downregulated in post-MPR samples compared to pre-MPR samples (Figure 1D). To validate this, we utilized another NSCLC NCIT dataset (GEO: GSE207422).[26] Major subclusters identified in GEO: GSE207422 were well-mapped to the CAF subtypes in our dataset (Figures S1H and S1I). Due to the limited MPR patient cells in GEO: GSE207422 (73/1,063 CAFs), we focused on non-MPR patients. Besides, the fraction of apCAFs was larger in post-non-MPR samples compared to pre-non-MPR samples (Figure S1J). Additionally, the expression levels of CD74, histocompatibility complex, class II, DR alpha (HLA-DRA) and histocompatibility complex, class II, DR belta 1 (HLA-DRB1) were higher in post-non-MPR samples compared to pre-non-MPR samples (Figure S1K). However, whether the fraction of apCAFs was indeed upregulated in post-non-MPR samples remained unclear. We thus collected an additional NCIT cohort consisting of 14 samples for validation (Figure S2A). By integrating the in-house supplementary dataset and GEO: GSE207422 with our discovery dataset, we gathered an adequate sample size and found that apCAFs were the only subcluster to exhibit significant enrichment in post-non-MPR samples (Figures S2A–S2C). Moreover, Luo et al. proposed that apCAFs likely originate from macrophages, and we further corroborated their findings through trajectory analysis, demonstrating that apCAFs indeed share transcriptional similarities with macrophages (Figures S2D–S2G).

pre-MPR (left) or upregulated in post-non-MPR versus post-MPR (right) are marked in blue. Genes belonging to apCAF signature are bolded. Genes marked by red are well-established markers for apCAFs according to the literature.

(E) Tumor weights of LLC tumors. $n = 5$ mice per group, representative of three independent experiments. p value is calculated using unpaired Student's t test. Error bars show the mean and SEM.

(F) Representative flow cytometric scatterplots of apCAFs within PDTF from non-MPR and MPR patients before or after anti-PD1 (left), with quantification on the right. In the barplots, apCAF means PDPN$^+$HLA-DR$^+$ cells (gated from CAF). Data are representative of three different experiments. p value is calculated using paired Student's t test.

(G) Experimental design of the PDTF platform.

(H) Representative flow cytometric scatterplots of the transwell co-culture systems. Quantification barplot is on the right. Data are representative of three different experiments. p values are determined using unpaired Student's t test, and error bars show the mean and SEM.

During single-cell analysis, subcluster "contamination" can occur, although it is rare. We double-checked the expression of typical CAF markers on apCAFs, including Podoplanin (PDPN), COL1A1, and platelet-derived growth factor receptor alpha (PDGFRA) (Figure S3A), confirming that apCAFs are indeed a distinct subcluster of CAFs. Additionally, we conducted bulk RNA-seq on primary CAF cell lines derived from patients' tumors (Figure 1A). Using morphological analysis and quantitative reverse-transcription PCR (RT-qPCR), we ensured the purity of the CAFs (Figure S3B). Among these, there were 4 cell lines each for post-non-MPR and post-MPR. We created a signature by intersecting characteristic genes of apCAFs from the integrated single-cell dataset, naming it the "apCAF NCIT signature." Indeed, the apCAF NCIT signature was significantly upregulated in post-non-MPR compared to post-MPR (Figures S3C and S3D). Moreover, the apCAF NCIT signature also showed exclusive enrichment in post-non-MPR specimens within SMA^+ CAFs as revealed by DSP spatial sequencing (Figures S3E and S3F).

In summary, through multi-omics analysis, we identified a specific CAF subcluster, apCAFs, as a potential indicator of post-non-MPR.

apCAFs expanded during immunotherapy and dampened anti-PD1 efficacy

Although our *in silico* analysis suggested that apCAFs might have expanded in post-non-MPR samples, its direct influence on immunotherapy efficacy and the factors responsible for its expansion remained unclear. We first conducted multiplexed immunofluorescence (mIF) to profile the distribution pattern of apCAFs. Notably, apCAFs were enriched in non-MPR samples compared to MPR samples. Moreover, after NCIT, the number of apCAFs was upregulated in post-non-MPR compared to pre-non-MPR. (Figure S3G).

Next, we constructed an orthotopic Lewis lung carcinoma (LLC) lung tumor model in C57BL/6 mice and sorted apCAFs and non-apCAFs from the tumors on day 27. These CAFs were mixed with LLC cells, followed by the construction of subcutaneous tumor models (Figure S3H).[27] We noticed that tumor growth curves were unaffected by non-apCAFs (Figures 1E, S3I, and S3J). Besides, apCAFs alone, without anti-PD1 intervention, did not exhibit pro-tumorigenic effects (Figures 1E and S3I). On the contrary, apCAFs significantly accelerated tumor growth during anti-PD1 regimens (Figures 1E, S3I, and S3J). Additionally, the granzyme B (GZMB) degranulation of $CD8^+$ TILs was dampened by apCAFs as well (Figure S3K). This indicated that apCAFs could directly dampen the efficacy of anti-PD1 therapy. Nevertheless, LLC is considered insensitive to anti-PD1 therapy, and, in our study, anti-PD1 treatment indeed failed to induce significant tumor shrinkage (Figures 1E and S3I). Therefore, we utilized two additional cell lines, SJT1601 and $Kras^{G12D}Tp53^{-/-}$ (KP), both of which have been reported to respond to anti-PD1 therapy. Using the same methodology as in the LLC models, we demonstrated that, in anti-PD1-sensitive tumor models, apCAFs significantly induced immunotherapy resistance (Figure S4). In contrast, in non-apCAF settings, tumor growth remained largely unaffected, regardless of anti-PD1 treatment (Figure S4).

However, *in vivo* models could not provide insights into the driving force behind apCAF expansion during NCIT. We then questioned whether apCAFs could be stimulated during anti-PD1 treatments. To explore this, we adopted an *ex vivo* 3D platform naming as patient-derived tumor fragments (PDTFs).[28] PDTFs were encapsulated in the same hydrogel used in the 3D culture of CAFs, and multiplexed flow cytometry (mFC) was conducted on them after 48 h of anti-PD1 treatment (Figures 1F–1H). We found that post-non-MPR samples had the largest fraction of apCAFs at baseline (Figures 1F and S5A). Furthermore, anti-PD1 treatment significantly enhanced apCAF expansion in both pre-non-MPR and post-non-MPR samples, but not in MPR samples (Figures 1F and S5A).

To determine whether direct contact or soluble factors led to apCAF marker upregulation, we first sorted CAFs and non-CAFs and then used the transwell assay to profile changes in apCAFs (Figures 1G and 1H). Besides, non-CAFs could stimulate apCAF accumulation in a non-contact manner (Figure 1H). Additionally, supernatants from non-CAFs had the same effect (Figures 1F–1H). Moreover, the non-MPR-specific expansion of apCAFs was also effectively recapitulated in CAFs cultured with supernatants from non-CAFs (Figure S5B).

In summary, we concluded that anti-PD1 directly stimulated apCAF expansion in non-MPR samples, and apCAFs served as a direct cause of resistance to immunotherapy.

Anti-PD1 stimulated apCAF expansion dependent upon overexpressed IFN-γ in non-MPR

Although we discovered that apCAF accumulation in post-non-MPR samples was dependent on anti-PD1 treatment, the specific pathway responsible remained unclear. Re-analysis of scRNA-seq data revealed that IFN receptors, such as interferon alpha and beta receptor subunit 2 (IFNAR2) (for type I IFN), interferon-gamma receptor 1/2 (IFNGR1/2) (for type II IFN), and IL-10RB (for type III IFN), were significantly upregulated in apCAFs compared to non-apCAFs (Figure 2A). Pathway enrichment analysis confirmed that IFN-related pathways were upregulated in apCAFs (Figure 2B), verified by gene set enrichment analysis (GSEA) in the NCIT dataset GEO: GSE207422 (Figure 2C). Additionally, in the previously described bulk RNA-seq of CAFs and DSP spatial sequencing data, the IFN-γ pathway also showed significant enhancement in post-non-MPR samples (Figures 2D and 2E).

To verify the *in silico* findings, we collected supernatants from PDTF culture for ELISA profiling (Figures 2F and 2G). Indeed, all three types of IFN, including IFN-α/β, IFN-γ, and IFN-λ, showed upregulation in the post-non-MPR PDTF supernatants (Figure 2F). We then transitioned from *ex vivo* to *in vitro* assays. We used the previously described human primary CAF biobank for downstream experiments (Figure 2G). We found that traditional 2D culture settings largely lost HLA-DRA expression compared to PDTF at the baseline time point. Meanwhile, 3D culture of CAFs could recover HLA-DRA expression (Figure 2H). Previous reports have also noted that CAFs lose MHCII molecule expression in 2D settings,[29] emphasizing the necessity of our 3D culture system. Regardless of the culture method, IFN-γ, but not IFN-α/β or IFN-λ, was the major IFN responsible for apCAF expansion, as confirmed by immunocytochemistry (ICC) (Figures 2I and 2J). As previously mentioned, we showed that anti-PD1 could enhance apCAF expansion. Using an

CellPress
OPEN ACCESS

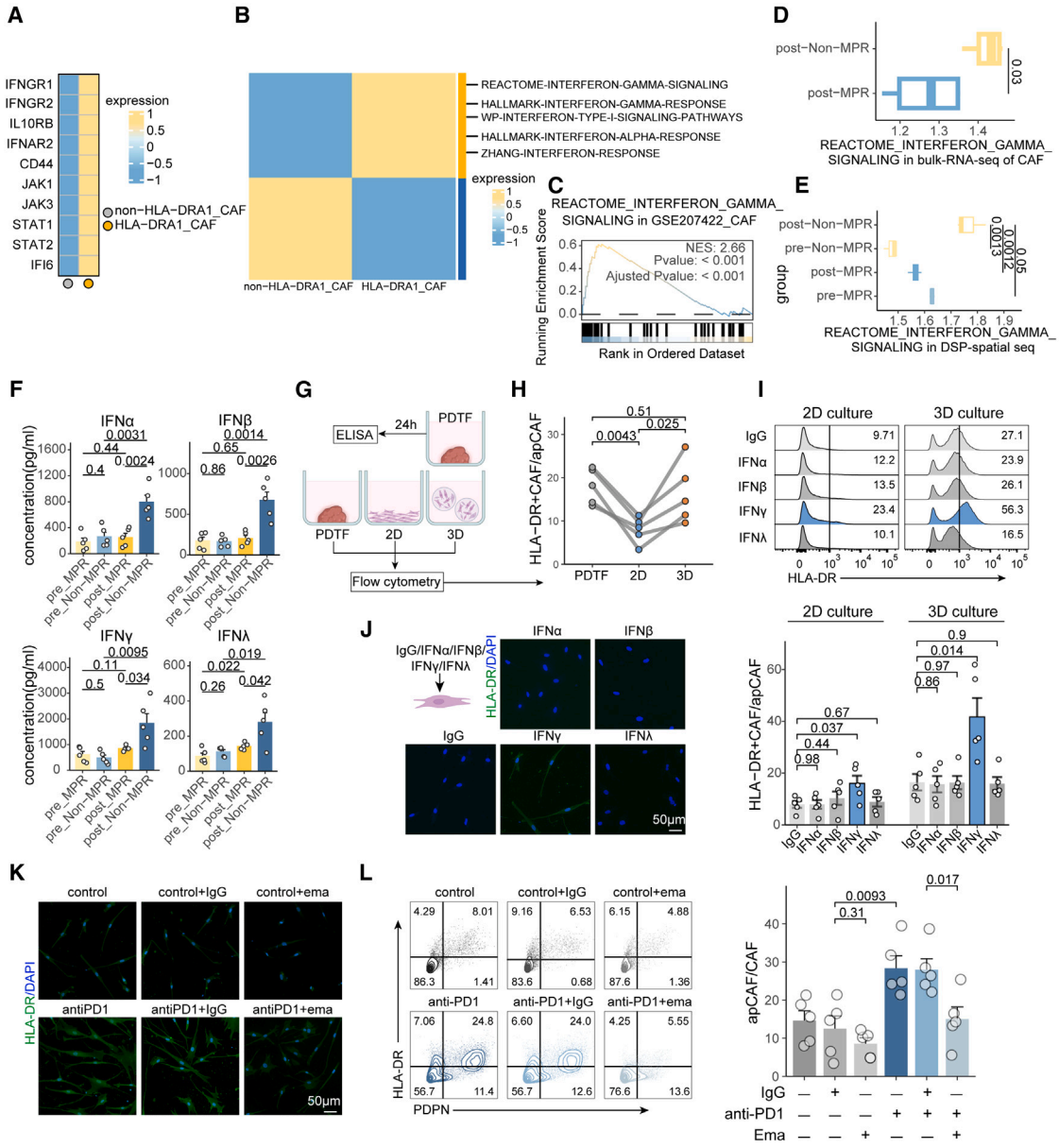

Figure 2. Anti-PD1-stimulated apCAF expansion is dependent upon IFN-γ

(A) IFN-related gene expression in apCAFs or other CAFs in our own NSCLC cohort.

(B) Heatmap showing scaled gene sets scores in apCAFs and non-apCAFs in our own NSCLC cohort.

(C) GSEA plot for REACTOME_INTERFERON_GAMMA_ SIGNALING in apCAFs in the GEO: GSE207422 cohort.

(D and E) Scores of REACTOME_INTERFERON_GAMMA_ SIGNALING in our bulk RNA-seq of CAFs (D) and our DSP dataset (E). *p* value is calculated using paired Student's t test.

(F) The concentration of interferons (IFNs) in supernatants of PDTF.

(G) Experimental design of the PDTF and 2D and 3D culture.

(H) The frequency of HLA-DR$^+$CAFs under the conditions of PDTF and 2D and 3D culture (G).

(I) Representative ridge plots of HLA-DR$^+$CAFs with the treatment of IFNs under the condition of 2D and 3D culture (upper) and quantification barplot (lower).

(J) Representative immunocytochemistry (ICC) pictures of HLA-DR$^+$CAFs with different treatments. Scale bar, 50 μm.

(K) Representative ICC pictures of HLA-DR$^+$CAFs with different treatments. Scale bar, 50 μm.

(L) Representative flow cytometric scatterplots of CAFs with different treatments (left) and the quantification barplot (right).

For (F), (H), (I), and (L), data are representative of three different experiments. *p* values are determined using unpaired Student's t test, and error bars show the mean and SEM.

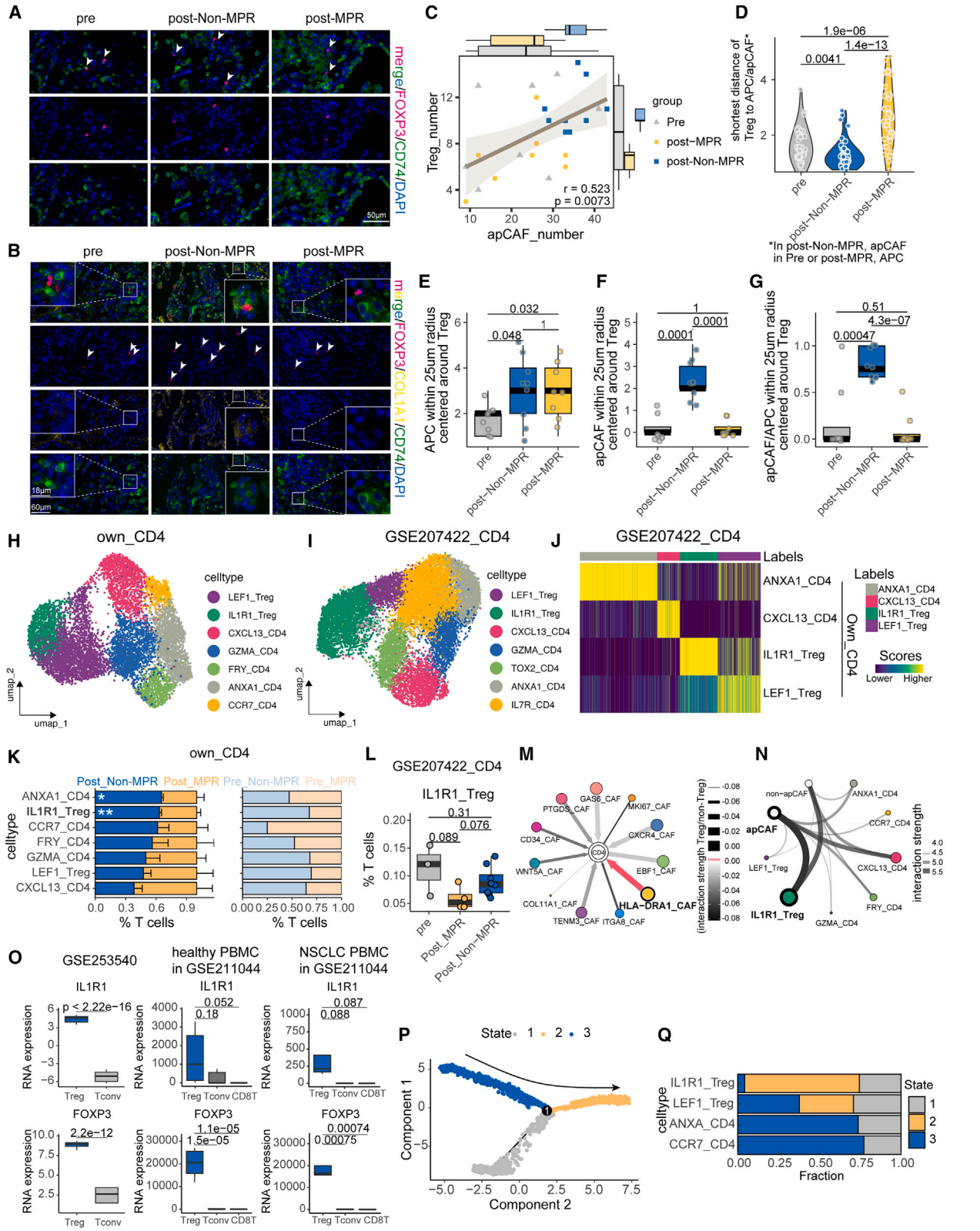

(legend on next page)

IFN-γ neutralizing antibody (emapalumab), we further confirmed that IFN-γ was necessary for the stimulation of apCAFs by anti-PD1 (Figures 2K and 2L). Supplementation with emapalumab largely blocked the upregulated apCAF fraction following anti-PD1 treatment, as corroborated by ICC (Figures 2K and 2L). To further investigate whether IFN-γ contributes to apCAF expansion *in vivo*, we generated primary apCAFs with stable interferon-gamma receptor (IFNGR) knockdown (KD), negative control knockdown (NCKD) group and utilized the previously described co-transplantation models for validation (Figure S5C). Compared to NCKD, KD apCAFs exhibited reduced expansion under anti-PD1 treatment (Figure S5I). Moreover, KD largely abolished apCAF-mediated resistance to anti-PD1 *in vivo* (Figures S5E–S5H), indicating that the IFN-γ-IFNGR axis plays a critical role in anti-PD1-induced apCAF expansion.

Although we concluded that the anti-PD1-IFN-γ axis was responsible for the expansion of apCAFs and that apCAFs served as important mediators of anti-PD1 resistance, the widespread expression of IFN-γ and IFNGR1/2 posed challenges for developing drugs targeting the "origin" of apCAFs due to the risk of off-target effects. Therefore, after addressing the questions of "what are apCAFs" and "where do they come from," we set out to investigate "where do they go," aiming to identify "targetable" axes centered around apCAFs.

Spatial co-localization of apCAFs with Tregs indicated their potential interactions

Using CellChat analysis, we found that CAFs exhibited the strongest cell-cell communication among major cell types within the TME (Figure S5J). We hypothesize that apCAFs contribute to ICI resistance through interactions with other cell types. TILs, the primary ICI responders, showed stronger interaction with apCAFs than non-apCAFs (Figure S5K), including CD8 TILs and Tregs. We previously proposed that non-CAF-secreted IFN-γ was responsible for apCAF expansion. Here, we identified a certain CD8 subtype, BAG3$^+$ T cells, as the most probable source of IFN-γ (Figures S5M–S5S). Additionally, compared to other known interaction partners of Tregs, such as macrophages and tumor cells, apCAFs exhibited even more interactions (Figure S5L). Brekken et al. found that apCAFs from mice orthotopic PDAC tumors could lead to Tregs formation in *in vitro* assays.[17] However, such immune-modulating effects have not been reported in other tumors or in *in vivo* scenarios. We hypothesized that apCAFs might also induce Tregs formation in the NSCLC TME. First, we tested if apCAFs were closely located near Tregs. Using mIF, we found that Tregs were more prevalent in post-non-MPR compared to pre- or post-MPR (Figure S6A) and were in direct contact with antigen-presenting cells (APCs) (CD74$^+$ cells) (Figure 3A), which are indispensable for Tregs differentiation.[30] While apCAFs are considered non-classic APCs,[17] the number of Tregs was positively correlated with the number of apCAFs (Figures 3B and 3C), which is not the case for non-apCAFs (Figure S6B). In post-non-MPR samples, the distances between Tregs and apCAFs were much shorter (Figures 3D and S6C), which is not observed in non-apCAFs either (Figure S6D). Although the number of APCs within a 25 μm radius around Tregs showed no difference between post-non-MPR

Figure 3. The spatial proximity of apCAFs and Tregs suggests potential communications between them

(A) Representative multiplexed IF (mIF) pictures of pre, MPR, non-MPR lung tumors, showing the spatial distributions of APCs (CD74$^+$) and Tregs (FOXP3$^+$). Arrows indicate the interaction between Treg and apCAFs. For each group, at least 4 patients were included. Scale bar, 50 μm.

(B) Representative mIF pictures showing the distributions of apCAFs (COL1A1$^+$CD74$^+$) and Treg (FOXP3$^+$). For each group, at least 4 patients were included. Arrows indicate the spatial distribution of Treg. Scale bar, 60 μm.

(C) Scatterplot showing the relationships between the number of Tregs and apCAFs in (B), colored by groups. Only visions with comparable DAPI$^+$ cells were selected for calculation. Each dot represents a vision. For each group, at least 4 patients were included; for each patient, at least 3 visions with Tregs were selected randomly. The correlation coefficient is calculated by Pearson, and *p* value is determined by two-sided linear regression t test.

(D) Violin plot showing the shortest distance of Treg to apCAFs/APC in (B). The shortest distance was determined by the distance between the apCAFs closest to a specific Treg. Only visions with comparable DAPI$^+$ cells were selected for calculation. Each dot represents a Treg cell. For each group, at least 4 patients were included; for each patient, at least 3 visions with Tregs were selected randomly; for each vision, every Treg was designated a shortest distance value. Significance was determined using unpaired Student's t test.

(E–G) (E) Boxplots showing the numbers of APCs within 25 μm radius centered around Tregs in (A). Only visions with comparable DAPI$^+$ cells were selected for calculation. (F) Boxplots showing the numbers of apCAFs within 25 μm radius centered around Treg in (B). Data are representative of three different experiments. (G) Boxplots showing the numbers of apCAFs/APCs within 25 μm radius centered around each Treg in (B). For (E)–(G), each dot represents a Treg cell. For each group, at least 4 patients were included; for each patient, at least 3 visions with Tregs were selected randomly; for each vision, at least one Treg was adopted to calculate the value. *p* value is calculated using unpaired Student's t test.

(H) UMAP plot of 9,363 CD4$^+$T cells colored by clusters in our NSCLC cohort.

(I) UMAP plot of 13,893 CD4$^+$T cells colored by clusters in the GEO: GSE207422 cohort.

(J) Heatmap showing the correlations between CD4$^+$T cells in our own CAF cohort and GEO: GSE207422 calculated by SingleR.

(K) The proportions of CD4$^+$T cell clusters. Significance was determined using unpaired Student's t test, and the absence of significance indicates no significant difference. $^*p < 0.05$, $^{**}p < 0.01$.

(L) The proportions of IL-1R1_Treg in different efficacy groups from the GEO: GSE207422 cohort. *p* value is calculated by unpaired Student's t test.

(M) Network graphs representing the relative interaction strength between CAFs and CD4$^+$ T cells (Treg and non-Treg).

(N) Network graphs representing the interaction between CAFs (apCAFs and non-apCAFs) and CD4$^+$ T cells. Edge strength represents the interaction strength calculated by CellChat.

(O) Expression of FOXP3 and IL-1R1 in Treg and Tconv in GEO: GSE253540 datasets (left). Expression of FOXP3 and IL-1R1 in Treg, Tconv, and CD8$^+$T in PBMC of the healthy donors or NSCLC patients from GEO: GSE211044 datasets (middle, right). *p* value is calculated using unpaired Student's t test.

(P) Monocle trajectory inference for IL-1R1_Treg, LEF1_Treg, ANXA1_CD4, and CCR7_CD4, colored by cell states. Analysis was conducted on our own CAF scRNA-seq data.

(Q) Proportion of cell state in each cluster.

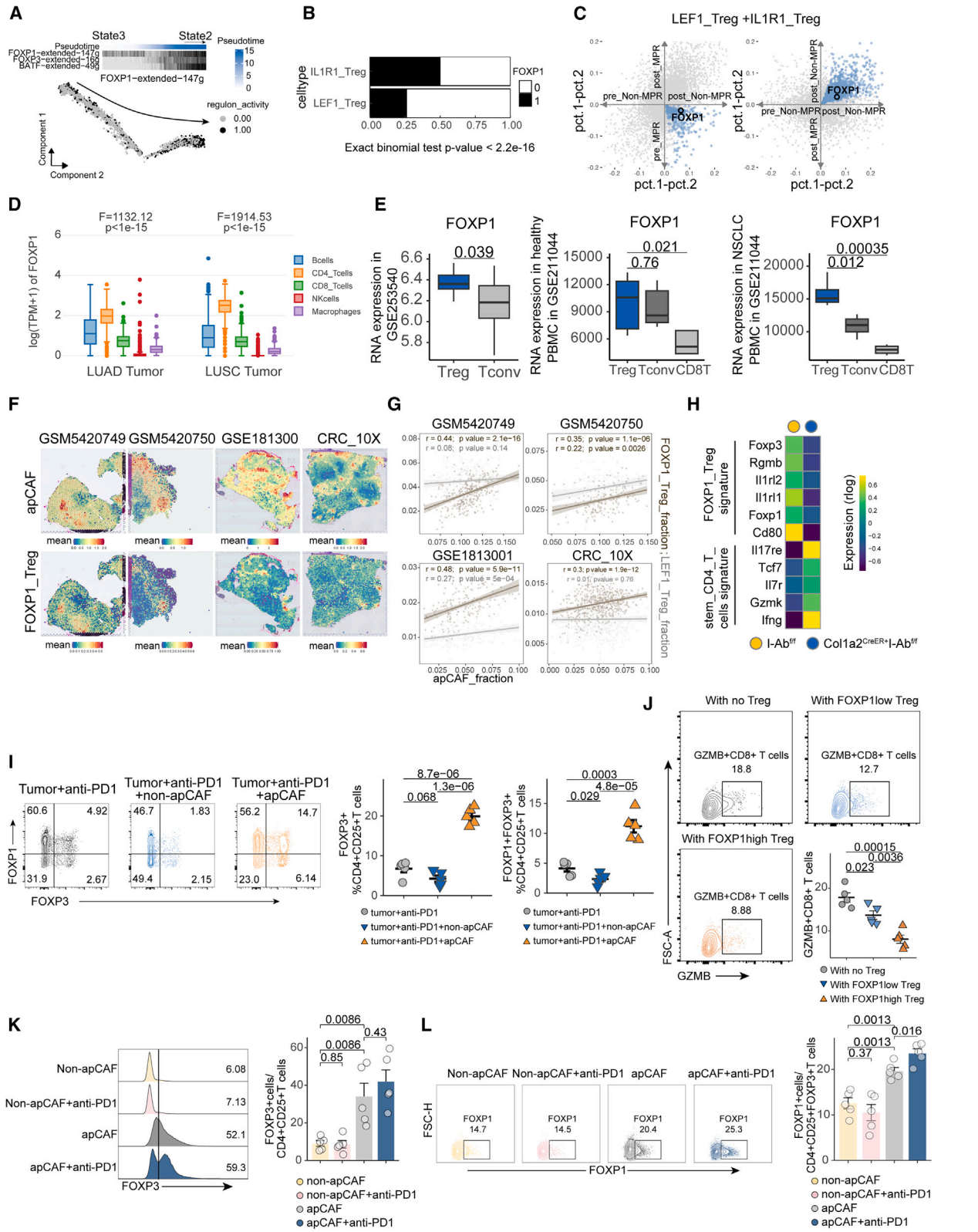

(legend on next page)

and post-MPR (Figure 3E), the number of apCAFs and the ratios of apCAFs to APCs were significantly higher (Figures 3F and 3G). Thus, among all APCs, apCAFs likely played a more important role in Treg formation in post-non-MPR compared to post-MPR or pre.

The advent of scRNA-seq has revealed significant heterogeneity in TME-infiltrated Tregs.[31] Ley et al. identified a cytotoxic Tregs subset (exTreg) that promotes pro-inflammatory responses rather than suppressing them.[32] Therefore, a detailed analysis of Tregs is necessary to identify the specific subtypes interacting with apCAFs. We closely examined the $CD4^+$ TILs and found that, among the seven well-distinguished subclusters (Figures 3H, S6E, and S6F), five were also present in the $CD4^+$ TILs from GEO: GSE207422,[26] showing excellent similarity (Figures 3I, 3J, and S6G). We then found that IL-1R1_Tregs were exclusively enriched in non-MPR both in our dataset and in GEO: GSE207422 (Figures 3K, 3L, and S6H). In contrast, another Tregs subtype, LEF1_Tregs, showed no significant changes in either dataset (Figures 3K and S6H). Therefore, we concluded that IL-1R1_Tregs, not LEF1_Tregs, is an important marker of non-MPR.

Nevertheless, the potential interactions between IL-1R1_Tregs and apCAFs remained unclear. Using our previously developed cell-communication pipeline, we found that apCAFs were the only subset showing enhanced communication with Tregs compared to non-Tregs (Figure 3M). Furthermore, apCAFs demonstrated stronger communication with IL-1R1_Tregs compared to non-apCAFs (Figure 3N), indicating potential interactions. IL-1R1_Tregs is a newly discovered suppressive $CD4^+$ subset.[33] We uncovered, using publicly available datasets,[34,35] that IL-1R1 is specifically expressed on Tregs from NSCLC patients' PBMC both *in vitro* and *ex vivo* (Figure 3O). To distinguish IL-1R1_Tregs from LEF1_Tregs, we conducted pseudotime analysis and found that LEF1_Tregs is a transitional subcluster along the differentiation trajectory from naive $CD4^+$ T cells (ANXA1_CD4 and CCR7_CD4) to IL-1R1_Tregs (Figures 3P–3Q). Interestingly, IL-1R1_Tregs was predominant in state 2, which showed higher expression of exhaustion markers (Figures 3Q, S6I–S6K, S7A, and S7B). However, IL-1R1 expression on Tregs was undetectable in our LLC mice models and Prlic et al.'s head and neck squamous cell carcinoma (HNSCC) mouse models,[33] likely due to potential intratumoral microbiome colonization. This dilemma remains unresolved, prompting us to consider surrogate markers for IL-1R1_Tregs through other multimodal analyses to better investigate apCAF-Tregs relationships *in vivo*.

apCAF-stimulated Tregs were characterized by FOXP1 expression

To identify markers equivalent to IL-1R1, we used single-cell regulatory network inference and clustering (SCENIC) analysis to pinpoint intrinsic transcription factors (TFs) driving IL-1R1_Tregs differentiation (Figure S7C). Notably, as cells transitioned from state 3 (dominated by naive $CD4^+$ TILs) to state 2 (dominated by IL-1R1_Tregs), FOXP1 activity increased (Figure 4A). Additionally, FOXP1 was more active in IL-1R1_Tregs compared to LEF1_Tregs (Figure 4B) and showed significantly higher expression in post-non-MPR samples (Figure 4C). Since FOXP1 can be reliably detected in mouse LLC models, we used $FOXP1^+$Tregs as a surrogate for IL-1R1_Tregs.

FOXP1 is crucial for FOXP3-mediated expression of CTLA-4 and CD25 on Tregs.[36–38] Deleting FOXP1 in $FOXP3^+$ Tregs leads to spontaneous inflammatory diseases in mice.[38] However, the biological roles of $FOXP1^+$ Tregs in tumor immunology remain largely unknown. First, we examined whether FOXP1 is exclusively expressed on $CD4^+$ TILs in the NSCLC TME. Deconvolution analysis of The Cancer Genome Atlas (TCGA) data showed that FOXP1 indeed has the highest expression in $CD4^+$ TILs (Figures 4D and S7D). Furthermore, Tregs exhibited significantly higher FOXP1 expression compared to conventional T cell (Tconv) or $CD8^+$ T cells in NSCLC PBMC (Figure 4E). We then investigated the spatial relationship between $FOXP1^+$ Tregs and apCAFs. Using publicly available spatial transcriptomics datasets[39–42] (ST-data), we found that the spatial distribution of apCAFs coincided with $FOXP1^+$ Tregs (Figure 4F). Additionally,

Figure 4. $FOXP1^+$Tregs specifically induced by apCAFs

(A) SCENIC-inferred TF activity of FOXP1, FOXP3, and BATF along the pseudotime trajectory.

(B) SCENIC-inferred TF activity of FOXP1 in IL-1R1_Treg and LEF1_Treg. *p* value is calculated by exact binomial test.

(C) Scatterplot showing gene expression change for post-non-MPR versus pre-non-MPR (x axis) against the post-MPR versus pre-MPR (y axis, left) or post-non-MPR versus post-MPR (y axis, right) in Treg. Genes significantly upregulated in post-non-MPR versus pre-non-MPR while downregulated in post-MPR versus pre-MPR (left) or upregulated in post-non-MPR versus post-MPR (right) are marked in blue. FOXP1 is bolded and highlighted.

(D) Expression of FOXP1 among immune cells from TCGA lung squamous cell carcinoma (LUSC) and lung adenocarcinoma (LUAD) datasets. *p* values are calculated using Wilcoxon test.

(E) Expression of FOXP1 in different cell types in GEO: GSE253540 datasets. *p* value is calculated using unpaired Student's t test.

(F) The coherence of apCAFs and IL-1R1_Treg in ST datasets. Spots are colored by the average expression of their markers relatively, selected from single-cell dataset.

(G) The correlation between fraction of apCAFs and IL-1R1_Treg (brown) or LEF1_Treg (gray) in spots from different ST datasets. The correlation coefficient is calculated by Pearson, and *p* value is determined by two-sided linear regression t test.

(H) Expression heatmaps (mean values) of genes from the IL-1R1_Treg and stem $CD4^+$ T cells signature in murine intratumoral lung $CD4^+$ T cells, purified from Col1a2 Cre^{ER+}I-$Ab^{fl/fl}$ versus I-$Ab^{fl/fl}$ mice and analyzed by bulk RNA-seq from GEO: GSE164659 datasets.

(I) Representative flow cytometric scatterplots of Treg in mice tumors, and the quantification of them, corresponding to the experiments in Figure 1E. Data are representative of three independent experiments. *p* values are determined using unpaired Student's t test, and error bars show the mean and SEM.

(J) Representative flow cytometric scatterplots of $GZMB^+CD8^+$ T cells and the quantification of them. Data are representative of three different experiments. *p* values are determined using unpaired Student's t test, and error bars show the mean and SEM.

(K and L) Representative ridge plots of Treg induced by apCAFs or non-apCAFs, with the treatment of anti-PD1, and the quantification.

For (I)–(L), data are representative of three different experiments. *p* values are determined using unpaired Student's t test, and error bars show the mean and SEM.

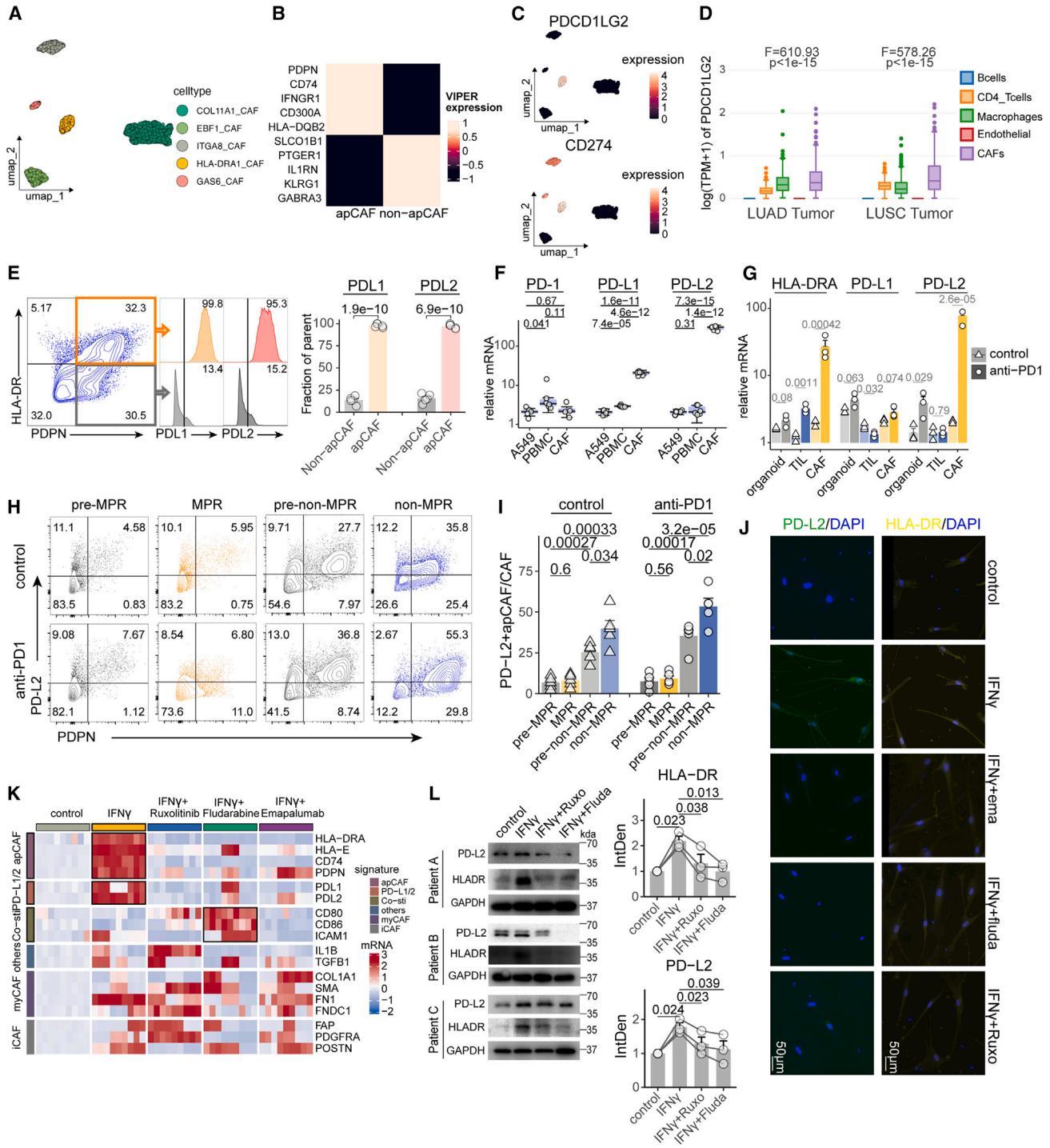

Figure 5. PD-L2 and HLA-DRA expression on apCAFs both under control of IFN-γ

(A) UMAP plot of CAFs colored by clusters in our NSCLC cohort based on the VIPER algorithm.

(B) Heatmap showing certain proteins' activity in apCAFs and non-apCAFs, calculated by VIPER.

(C) Feature plots of PDCD1LG2 and CD274 protein activity based on the VIPER metrics.

(D) Expression of PDCD1LG2 among immune cells from TCGA LUSC and LUAD datasets. *p* values are calculated using Wilcoxon test.

(E–G) (E) Representative flow cytometric histograms of expression of PD-L1 and PD-L2 in apCAFs and non-apCAFs, with quantification on the right. (F) PD1, PD-L1, and PD-L2 expression in tumor cells (A549), immune cells (PBMCs), and CAFs assessed by RT-qPCR. (G) mRNA expression level of genes quantified by

(legend continued on next page)

FOXP1$^+$ Treg fractions were more correlated with apCAF fractions in ST-data spots compared to LEF1$^+$ Tregs (Figure 4G).

We thus hypothesized that apCAFs might induce the expansion of FOXP1$^+$Tregs. Besides, compared to CD4$^+$ TILs from apCAF-knockout mice (Col1a2 CreER$^+$I-Ab$^{fl/fl}$), CD4$^+$ TILs from the control group (I-Ab$^{fl/fl}$) showed upregulation of FOXP1_Tregs signature genes (Foxp3, Il1rl1, Il1rl2, etc.) and diminished expression of stem CD4$^+$ T cells signature genes (Tcf7, Il7r, Gzmk, etc.) (Figure 4H), suggesting that apCAFs might directly stimulate FOXP1$^+$ Treg expansion *in vivo*. In co-transplantation models, the TME of apCAF-enriched tumors also exhibited significantly more FOXP1$^+$ Tregs, as well as a higher overall number of Tregs (Figures 4I and S7E). Tregs sorted from the TME of apCAF-enriched tumors (termed "FOXP1high Tregs") showed the strongest suppressive function on the cytotoxic behavior of CD8$^+$ TILs *ex vivo* (Figures 4J and S7F). We then co-cultured apCAFs or non-apCAFs sorted from patient-derived CAFs with corresponding autologous naive CD4$^+$ TILs. Additionally, Tregs, including FOXP1$^+$Tregs, exhibited substantial expansion in the apCAF co-culture groups, regardless of anti-PD1 stimulation (Figures 4K and 4L).

Taken together, we identified that FOXP1$^+$Tregs could well-represent IL-1R1$^+$Tregs and uncovered that apCAFs could directly stimulate FOXP1$^+$Treg expansion, both *in vivo* and *in vitro*.

Anti-PD1 induced exclusive expression of PD-L2 on apCAFs relying upon IFN-γ

The primary objective of our investigation into the interaction between apCAFs and FOXP1$^+$ Tregs was to identify "targetable" axes to counteract apCAFs-mediated NCIT resistance. We first examined whether neutralizing HLA-DRA expression on apCAFs could inhibit Tregs differentiation. Besides, αMHCII only partially reduced the effect of apCAFs on Tregs and FOXP1$^+$ Tregs, indicating that additional mechanisms were involved (Figure S8A). To explore potential mediators beyond MHCII, we conducted Virtual Inference of Protein-activity by Enriched Regulon (VIPER) analysis, a protein-activity quantification algorithm,[43] on our single-cell data of CAFs. The re-clustering of CAFs based on protein activity was highly consistent with transcriptomic data (Figures 5A and 5B). Crucially, VIPER-derived apCAFs uniquely expressed PD-L1 and PD-L2 (Figures 5A–5C). This finding was significant as Akbari et al. recently demonstrated that PD-L2 is crucial for Tregs maintenance and stability.[44] Thus, beyond MHCII/T cell receptor signaling, the co-inhibitory axis of PD-L1/2 may also contribute to apCAF-mediated Tregs expansion. Despite the low RNA levels of PD-L1/2 and the sparse nature of single-cell transcriptomics, which limited the identification of PD-L1/L2 on apCAFs, VIPER analysis successfully highlighted their presence. mFC analysis confirmed that apCAFs, rather than non-apCAFs, were indeed the primary CAF sub-cluster expressing PD-L1/L2 (Figure 5E).

We next questioned the biological value of PD-L1/2$^+$ CAFs. First, in TCGA lung cancer data, CAFs contribute comparable PD-L2 expression in the TME as macrophages, while this is not the case for PD-L1 (Figures 5D and S8B–S8D). Additionally, we found that CAFs manifested the highest PD-L1/2 expression compared to tumor cells and immune cells (Figure 5F). We then conducted RT-qPCR upon FACS-sorted organoids, CAFs, and TILs from the same individual. While anti-PD1 diminished PD-L1 expression on TILs, it significantly upregulated HLA-DRA and PD-L2 expression on both organoids and CAFs, with the latter showing a much greater increase (Figure 5G). Taken together, we suggested that CAFs were pivotal contributors to PD-L1/2 expression in the TME during anti-PD1 treatments.

Theoretically, anti-PD1 blocks PD1/L1-mediated effects, leading us to hypothesize that, in the case of NCIT resistance, PD-L2 might be responsible. TCGA analysis confirmed that PD-L1 expression is relatively low in CAFs (Figure S8D), and anti-PD1 treatment did not further up-regulate PD-L1 expression on CAFs (Figure 5G). Therefore, we focused on PD-L2 expression fluctuations in apCAFs using the previously mentioned PDTF obtained during NCIT. Additionally, PD-L2$^+$ apCAFs were significantly enriched in post-non-MPR specimens (Figures 5H and 5I). After anti-PD1 treatments *ex vivo*, their fractions increased further in both pre- and post-non-MPR (Figures 5H and 5I). As mentioned earlier, PD-L2 is exclusively expressed by apCAFs, whose expansion depends on IFN-γ. Since IFN-γ was reported to be responsible for PD-L2 expression on tumor cells, we investigated whether this was also the case for CAFs.[45] Additionally, IFN-γ significantly upregulated HLA-DRA and PD-L2 expression on CAFs (Figure 5K). Neutralization of IFN-γ, knockdown of IFNGR, or inhibition of JAK1/2 or STAT1 largely rescued these effects (Figures 5K and S5D). Notably, neither other CAF subsets such as inflammatory CAFs (iCAFs) and myofibroblast CAFs (myCAFs) nor co-stimulatory molecules (CD80/86) were controlled by the IFN-γ signaling pathways in CAFs (Figure 5K). Western blot (WB), ICC, and mFC analyses of patient-derived CAFs cell lines further corroborated our RT-qPCR findings (Figures 5J, 5L, and S8E). We further used a human fibroblast cell line (HFL1) and a

RT-qPCR for organoids, TILs, or CAFs with treatment of anti-PD1 or its isotype antibody. For (E)–(G), data are representative of three independent experiments. *p* values are determined using unpaired Student's t test, and error bars show the mean and SEM.

(H) Representative flow cytometric scatterplots of PDTF from non-MPR and MPR patients before or after anti-PD1 (left), with quantification in (I). Data are representative of three independent experiments.

(I) Frequency of PD-L2$^+$ apCAFs in PDTF. Data are representative of three different experiments. *p* values are determined using unpaired Student's t test, and error bars show the mean and SEM.

(J) Representative immunocytochemistry (ICC) pictures of HLA-DR$^+$CAFs/PD-L2$^+$CAFs with the supplement of IFN-γ, emapalumab, fludarabine, or ruxolitinib. Data are representative of three independent experiments. Scale bar, 50 μm.

(K) Heatmap showing the mRNA expression level assessed by RT-qPCR. Each specific column means a specific patient's CAF cell line. For every gene listed in the apCAFs and PD-L1/2 signatures, the difference between any two treatment groups is significant, determined by two-way ANOVA test.

(L) The protein expression levels of PD-L2 and HLA-DR in patients-derived CAFs measured by WB (left) and the integrated density of them measured by ImageJ. Data of three representative patients are posted here. *p* values are determined using unpaired Student's t test.

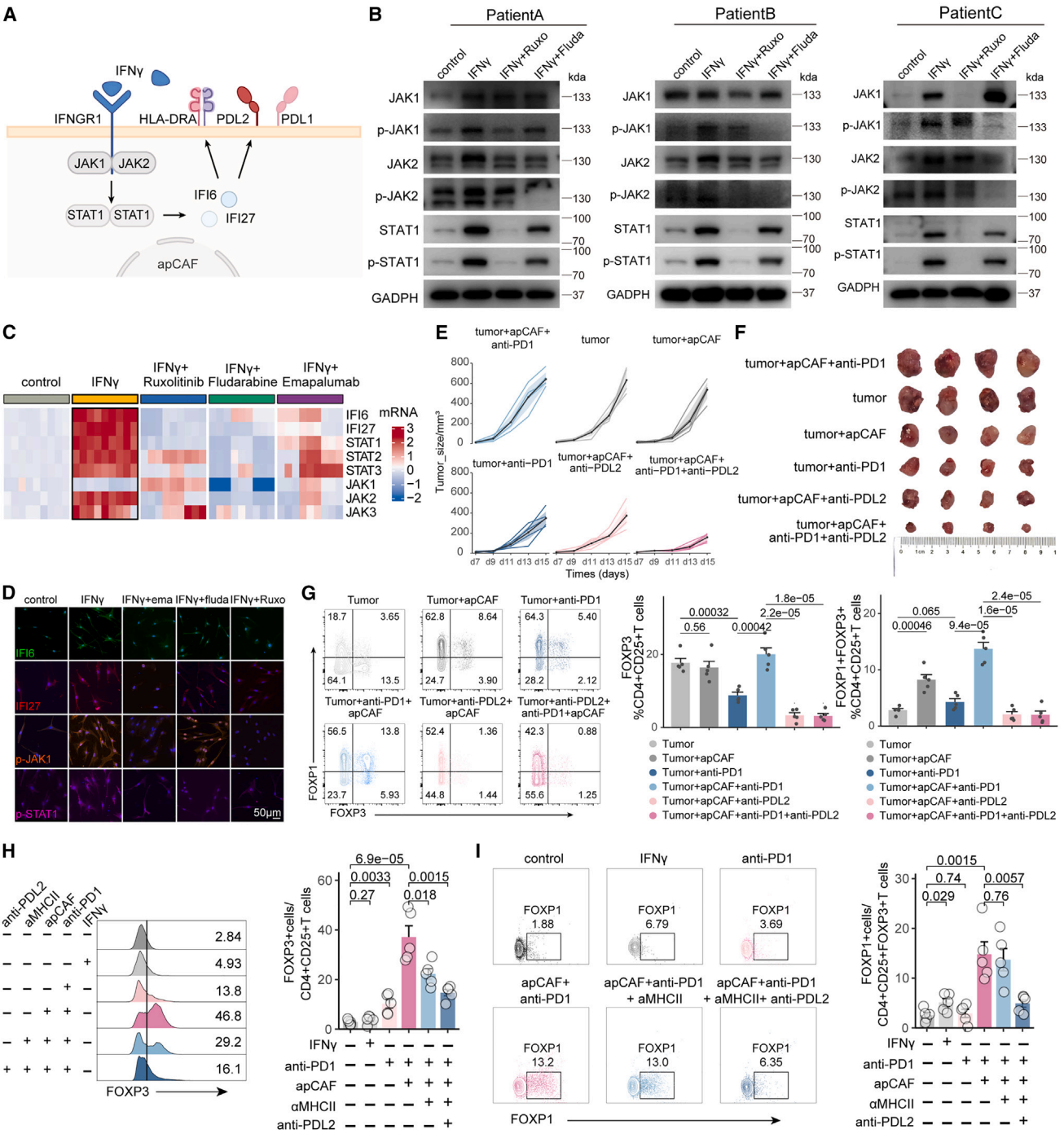

Figure 6. Disruption of the JAK1/2-STAT1-IFI6/27-PD-L2 axis in apCAFs to compromise FOXP1$^+$Tregs

(A) Diagram of mechanism of IFN-γ on apCAFs.

(B) The protein expression levels of JAK-STAT pathway. Data are representative of three independent experiments.

(C) Heatmap showing the mRNA expression level for genes from JAK-STAT pathway assessed by RT-qPCR. Each specific column means a specific patient's CAF cell line. For every gene, the difference between any two treatment groups is significant, determined by two-way ANOVA test.

(D) Representative ICC pictures of IFI6/27, p-STAT1, and *p*-JAK1 pathway. Scale bar, 50 μm.

(E) Tumor growth curves: tumor cells + apCAFs + anti-PD1 (light blue), tumor cells (light gray), tumor + apCAFs (gray), tumor + anti-PD1 (navy blue), tumor + apCAFs + anti-PD-L2 (pink), and tumor + apCAFs + anti-PD1 + anti-PD-L2 (magenta). Individual and mean tumor volume over time. *n* = 5 mice per group, representative of three independent experiments.

(F) The tumor photos of mice in (E). *n* = 4 mice per group.

(legend continued on next page)

murine fibroblast (MF) to double-check our results, which remained consistent (Figures S8F and S8G). Altogether, we concluded that anti-PD1 stimulated PD-L2$^+$apCAFs expansion in an IFN-γ-dependent manner, offering perspectives on apCAFs-Tregs interactions.

Reprogramming apCAFs and anti-PD-L2 (clone 3.2) overcame anti-PD1 resistance

No detailed research has been conducted on the specific regulatory axis responsible for PD-L2$^+$apCAFs until now. We discovered that IFN-γ can stimulate PD-L2$^+$apCAFs via the JAK1/2-STAT1-IFI6/27 pathway (Figure 6A). Through WB and RT-qPCR analyses of patient-derived CAF cell lines, we confirmed that IFN-γ directly upregulated the phosphorylation of the JAK1/2-STAT1 pathway (Figures 6B and 6C). Ruxolitinib, a selective JAK1/2 inhibitor, significantly inhibited the total amount of JAK1/2 and STAT1 protein expression, as well as their phosphorylation (Figures 6B and 6C). Similarly, fludarabine, a STAT1 activation inhibitor, showed the same effects (Figures 6B and 6C). Additionally, emapalumab, an IFN-γ neutralization antibody, reduced JAK1/2-STAT1-IFI6/27 expression at the RNA level to some extent (Figure 6C). We further verified these findings in the HFL1 cell line (Figures S9A and S9B). We previously identified IFI6/27 as markers of apCAFs through multi-omics analysis, which were traditionally considered downstream responders to IFN-α/β-mediated STAT1 activation.[46] However, few studies have reported their correlation with IFN-γ signaling. Using RT-qPCR and ICC, we confirmed that JAK1/2-STAT1 also controls the expression of IFI6/27 (Figures 6C and 6D). On the other hand, since the JAK3-STAT3 axis is also under IFNs' control and receptors for IFNα/β were exclusively enriched in apCAFs, we questioned whether there could be bypass activation of STAT3 or IFNα/β receptors signaling pathways in PD-L2$^+$apCAFs. However, neither IFNAR1/2 inhibitors (anifrolumab and IFNAR-IN-1) nor the STAT3 inhibitor (NSC74859) could reverse the effects of IFN-γ (Figures S9C and S9D). Finally, inhibition of the IFN-γ-JAK1/2-STAT1 pathway significantly downregulated PD-L2 and HLA-DRA expression on CAFs (Figures 5J–5L). In general, we uncovered that the IFN-γ-JAK1/2-STAT1-IFI6/27 axis was responsible for PD-L2$^+$apCAF expansion.

Aforementioned work led us to identify interventions targeting apCAFs. Considering methods targeting the IFN-γ-JAK1/2-STAT1-IFI6/27 axis may not be cost-effective or easily translatable (Figures S10A–S10H), we next investigated whether anti-PD-L2 (clone 3.2) could overcome anti-PD1 resistance in an apCAF-enriched TME. Besides, anti-PD-L2 significantly decelerated tumor growth even in the presence of apCAFs (Figures 6E, 6F, S11A–S11C, and S11F–S11H). Furthermore, anti-PD-L2, or the combination of anti-PD-L2 and anti-PD1, largely rescued the expansion of FOXP1$^+$Tregs and total Tregs (Figures 6G, S11D, and S11I), resulting in reactivation of CD8$^+$ TILs (Figures S10H, S11E, and S11J). Interestingly, in *ex vivo* co-culture assays, although αMHCII could diminish Treg expansion to some extent, it had limited effects on FOXP1$^+$ Tregs (Figures 6H and 6I). In contrast, the addition of anti-PD-L2 further reduced Treg formation and significantly inhibited FOXP1$^+$Treg expansion, indicating that FOXP1$^+$Tregs might be specifically induced by the PD-L2 signaling pathway (Figures 6H and 6I). Moreover, both *in vivo* and *in vitro*, anti-PD-L2 combined with anti-PD1 restored the anti-tumor capacity of CD8$^+$ TILs, which was originally dampened by the apCAF-FOXP1$^+$Tregs axis. Altogether, we concluded that, since a considerable amount of PD-L2 was attributed to apCAFs, apCAF-enriched TME resistant to anti-PD1 could significantly benefit from the addition of anti-PD-L2 (clone 3.2).

The PD-L2-RGMB axis was indispensable for apCAFs-FOXP1$^+$Tregs interaction

Recently, Sharpe et al. identified RGMB as another indispensable binding partner of PD-L2.[22] They found that TILs from mice transplanted with gut microbiome from non-responders to anti-PD1 had higher expression of RGMB. The clone 3.2 of anti-PD-L2 blocks both PD-L2-RGMB and PD1-PD-L2 interactions, thus synergizing with anti-PD1.[22] We also found that, in an apCAF-enriched TME, anti-PD-L2 (clone 3.2) could significantly reverse resistance to anti-PD1. Since these effects were accompanied by a reduction in FOXP1$^+$Tregs, we hypothesized that RGMB might be involved in apCAFs-FOXP1$^+$Tregs communication.

Currently, the differences in RGMB expression among major clusters of TILs remain unclear. Interestingly, we found that CD4$^+$ TILs exhibited higher RGMB expression compared to B cells, CD8$^+$ T cells, or natural killer cells in the NSCLC TME (Figure 7D; Figure S12A). Additionally, Tregs showed significantly higher RGMB levels compared to Tconv and CD8$^+$ TILs (Figure 7B). This indicates that Tregs are the major contributors to RGMB expression among TILs. Next, our analysis of publicly available RNA-seq data of FOXP1^{KO} Tregs not only confirmed that FOXP1 is essential for FOXP3 but also revealed that FOXP1 might positively regulate RGMB (Figure 7C). We verified these findings through mFC analysis, which showed that CD4$^+$ TILs indeed exhibited significantly higher RGMB expression (Figure 7E). Although apCAFs did not up-regulate RGMB expression on FOXP1$^+$Tregs (Figure 7G), RGMB expression on FOXP1$^+$Tregs was notably higher than that on FOXP1$^-$Tregs (Figure 7F). Furthermore, anti-PD1 treatment increased the fraction of RGMB$^+$Tregs (Figure 7G). Finally, we observed increased chromatin accessibility of RGMB, IL-1R1, and FOXP1 in Tregs compared to CD8$^+$ T cells or Tconv, highlighting their potential influence on Treg formation[34] (Figures 7H and S12B).

In the apCAF-enriched TME, anti-RGMB could also overcome resistance to anti-PD1 (Figures 7I–7K). When combined with anti-PD1 or anti-PD-L2 (clone 3.2), anti-RGMB significantly reduced tumor growth and volumes (Figures 7I–7K, S13A–S13C,

(G) Representative flow cytometric scatterplots of FOXP1$^+$Tregs in mice tumors and the quantification. *p* values are determined using unpaired Student's t test, and error bars show the mean and SEM.
(H and I) Representative ridge plots.
For (D)–(I), data are representative of three independent experiments. *p* values are determined using unpaired Student's t test, and error bars show the mean and SEM.

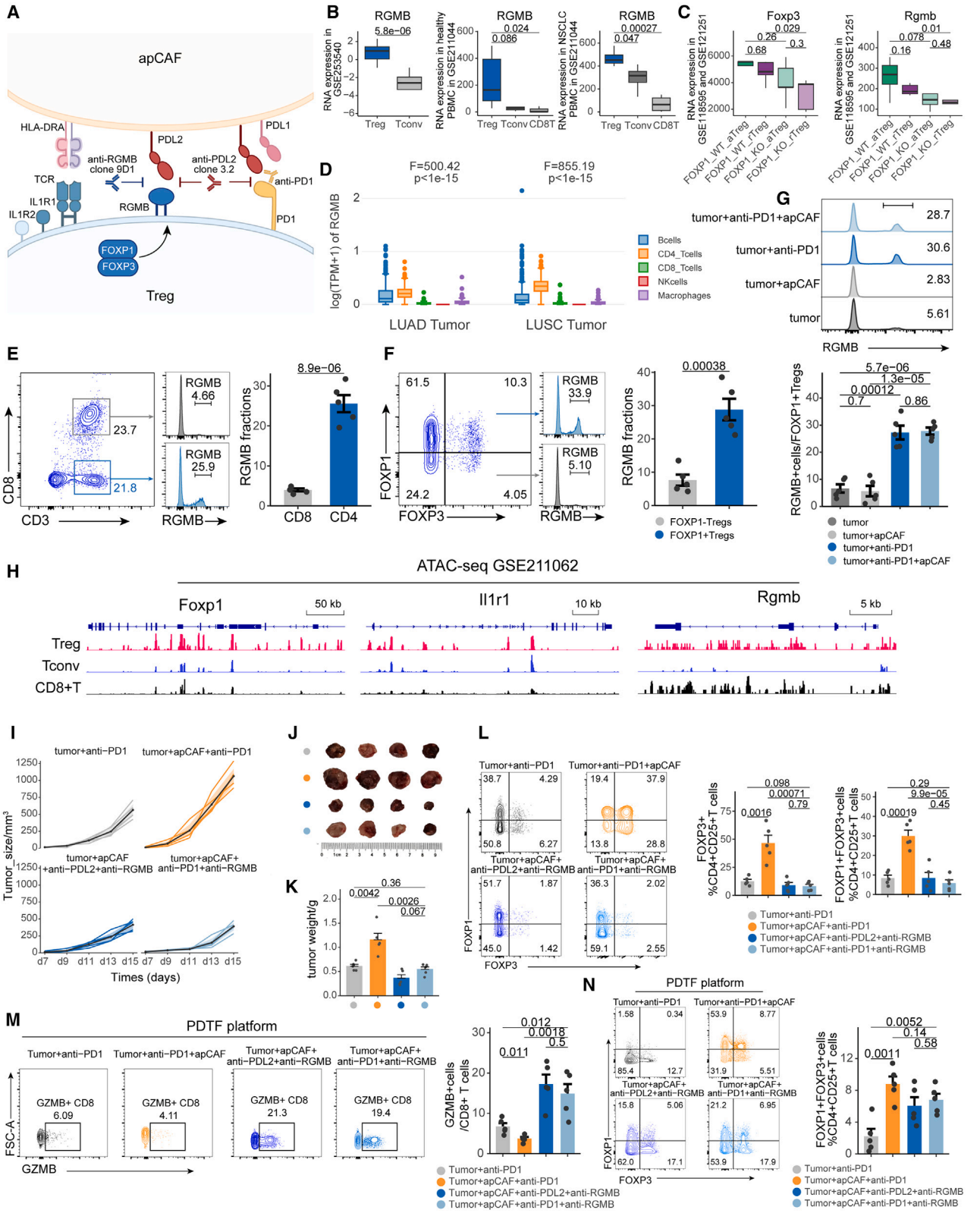

(legend on next page)

and S13F–S13H), as well as the fractions of FOXP1$^+$Tregs and total Tregs (Figures 7L, S12C, S13D, and S13I). Besides, either *in vivo* or in the PDTF platforms, the addition of anti-RGMB enormously increased GZMB secretion by CD8$^+$ TILs (Figures 7M, S13E, and S13J). Although the shrinkage of FOXP1$^+$Tregs under anti-RGMB was not significant *in vitro* (Figure 7N), likely due to the absence of the gut microbiome, we could still conclude that anti-RGMB together with anti-PD1/L2 managed to successfully overcome apCAF-mediated resistance to anti-PD1.

DISCUSSION

NCIT has provided a valuable opportunity to investigate the mechanisms underlying immunotherapy resistance. Accordingly, we conducted a multi-omics analysis of NSCLC patient samples treated with NCIT. Our focus on CAFs led to the identification of apCAFs as key mediators of the resistance to NCIT.

Although apCAFs had been previously identified, the mechanisms of their formation remained poorly understood. In PDAC, apCAFs were thought to differentiate from mesothelial cells.[17] Later, Jiang et al. demonstrated that IL-1R2$^+$Tregs could maintain apCAFs by inhibiting IL-1-IL-1R1 signaling in colon cancers.[18] However, our single-cell data of NSCLC revealed comparable IL-1R1 expression on both Tregs and apCAFs, suggesting that additional factors are involved. Using 3D culture settings,[20] we identified IFN-γ as another crucial mediator of apCAF expansion. Furthermore, we clarify that the JAK1/2-STAT1-IFI6/27 axis is the primary pathway driving apCAF expansion. This finding significantly advances the understanding of apCAFs.

IFNs have traditionally been considered crucial to anti-tumor immunity.[47] On the contrary, we found that IFN-γ can reduce NCIT efficacy by specifically stimulating apCAFs. This discovery stemmed from observing increased IFNs in post-non-MPR samples, which might seem counterintuitive since IFNs are typically considered markers of "hot" tumors. However, recent studies demonstrate that "hot" tumors are actually more susceptible to acquired immunotherapy resistance.[48] For example, IFN-γ can promote Yes-associated protein (YAP) phase separation in cancer cells,[49] leading to resistance to anti-PD1. What is more, Hellmann et al. found persistent IFN-γ signaling in the TME of stage IV NSCLC patients with acquired anti-PD1 resistance.[50] Our research further confirms that the IFN-γ-apCAF axis contributes to NCIT resistance in stage I/II NSCLC as well. Both our study and Hellmann et al.'s[50] support the idea that a persistently inflamed, rather than immune-desert, TME might drive acquired immunotherapy resistance.

We further identified a potential mechanism of IFN-γ-mediated immunotherapy resistance: the exclusive expression of PD-L2 on apCAFs. PD-L2$^+$ CAFs manifested cancer-type-specific, context-dependent roles. PD-L2 expressed by CD29$^+$ FAP$^+$ CAFs mediate Treg retention in breast cancer,[51] while PD-L2$^+$CAFs accelerate CD8$^+$ T cells' apoptosis in melanoma.[52] However, the relationship between apCAFs and PD-L2 in NSCLC was still unclear. We revealed that apCAFs, not other CAF subtypes, are the primary source of PD-L2 in the NSCLC TME. Although anti-PD1 blocked the PD1/PD-L2 axis, the PD-L2/RGMB axis emerged to dampen anti-PD1 efficacy. Sharpe et al. reported that RGMB on T cells contributes to T cell anergy.[22] We further confirmed that FOXP1$^+$Tregs are the main contributors to RGMB within TILs. FOXP1 is indispensable for FOXP3 chromatin accessibility and Treg homeostasis.[36–38] However, the role of FOXP1 in Tregs within the context of NCIT was previously unknown. We discovered that FOXP1 acts as a TF marker for a post-non-MPR-responsive Treg subcluster, IL-1R1$^+$Tregs, and may positively regulate RGMB expression on Tregs. Interestingly, as previously reported, FOXP1 could facilitate CTLA-4 expression on Tregs,[38] and RGMB binding enhanced its suppressive activity.[53] Taken together, we believed that, as the "executioner" of

Figure 7. Blockade of PD-L2-RGMB interaction to overcome anti-PD1 resistance both *in vivo* and in PDTF platforms

(A) Diagram of interaction between apCAFs and Treg.

(B) Expression of RGMB in GEO: GSE253540 datasets (left).

(C) Expression of Foxp3 and RGMB in aTreg (activated Tregs) and rTreg (rested Tregs) either with knockout (KO) of FOXP1 or not in the merged GEO: GSE118595 and GEO: GSE121251 datasets.

(D) Expression of RGMB among immune cells from TCGA and LUAD datasets. *p* values are calculated using Wilcoxon test.

(E) Expression of RGMB in CD4$^+$T cells and CD8$^+$T cells. Data are representative of three independent experiments. *p* values are determined using unpaired Student's t test, and error bars show the mean and SEM.

(F) Expression of RGMB in FOXP1$^+$ and FOXP1$^-$ Tregs. Data are representative of three independent experiments. *p* values are determined using unpaired Student's t test, and error bars show the mean and SEM.

(G) Representative ridge plots of RGMB$^+$ cells (upper) and quantification (lower). Data are representative of three independent experiments. *p* values are determined using unpaired Student's t test, and error bars show the mean and SEM.

(H) Re-analyzation results for Foxp1, Il1r1, and RGMB in Treg, Tconv, or CD8$^+$ T cells in the GEO: GSE211062 assay for transposase-accessible chromatin by sequencing (ATAC-seq) dataset.

(I) Tumor growth curves: tumor + anti-PD1 (gray), tumor apCAFs + anti-PD1 (orange), tumor cells + apCAFs + anti-PD-L2 + anti-RGMB (blue), and tumor cells + apCAFs + anti-PD-L2 + anti-RGMB (light blue). Individual and mean tumor volume over time. n = 5 mice per group, representative of three independent experiments.

(J) The tumor photos of mice in (I). n = 4 mice per group.

(K) The tumor weight of mice in (I). n = 4 mice per group.

(L) Representative flow cytometric scatterplots of FOXP3$^+$Treg and FOXP1$^+$FOXP3$^+$Treg in mice tumors in (I) (left) and the quantification of them (right). Data are representative of three different experiments. *p* values are determined using unpaired Student's t test, and error bars show the mean and SEM.

(M and N) Representative flow cytometric scatterplots of GZMB$^+$CD8$^+$T cells (M) and FOXP1$^+$FOXP3$^+$Tregs (N) in PDTF (left) and the quantification of them (right). For (B)–(C), *p* value is calculated using unpaired Student's t test. For (I)–(K), data are representative of three independent experiments, *p* values are determined using unpaired Student's t test, and error bars show the mean and SEM. For (L)–(N), data are representative of three independent experiments, and *p* values are determined using unpaired Student's t test and error bars show the mean and SEM.

apCAF-mediated resistance to NCIT, RGMB^{+}FOXP1^{+}Tregs warrant further investigation.

Lastly, our research highlights pivotal translational aspects and future research directions. First, in co-culture assays, we found that inhibiting the JAK1/2-STAT1 pathway in CAFs not only reduced PD-L2 expression but also restored CD80/86, thereby reversing FOXP1^{+} Treg expansion through co-stimulatory signaling. This suggests another potential strategy to counter apCAF-mediated resistance, though further *in vivo* validation is needed. For instance, the JAK1/2 inhibitor ruxolitinib has shown synergy with nivolumab in phase 1/2 trials for NSCLC and Hodgkin's lymphoma.[54,55] Thus, whether JAK1/2 inhibitors may also be able to reprogram apCAFs *in vivo* warrants further investigation. Finally, we also observed enrichment of apCAFs in pre-non-MPR, suggesting additional mechanisms for apCAF residency before anti-PD1 therapies. Given that apCAF expansion is IFN-γ dependent, we hypothesized that certain subclusters enriched in pre-non-MPR with high expression of IFN-γ might contribute to it and identified BAG3^{+}CD8^{+}TILs as a key source. Therefore, further investigation into the interplay between apCAFs and BAG3^{+}CD8^{+}TILs will be of great significance to further target apCAFs.

Limitations of the study

The central mechanism we identified—apCAFs driving immunotherapy resistance via FOXP1^{+} Treg induction—requires further contextualization within broader immune cell interactions. The role of apCAFs as non-professional APCs in modulating other immune cells, such as CD8^{+}T cells and dendritic cells (DCs), remains unclear. Therefore, future studies using advanced approaches, such as lineage-specific genetically engineered models, are essential to elucidate the cell-cell communication between apCAFs and immune cells beyond Tregs. These insights could uncover novel therapeutic targets beyond the PD-L2/RGMB axis and further enhance our understanding of apCAF-mediated resistance to neo-ICIs.

RESOURCE AVAILABILITY

Lead contact

Further information and requests for resources and regents should be directed to and will be fulfilled by the lead contact, Dr. Ziming Li (liziming1980@shsmu.edu.cn).

Materials availability

This study did not generate any new unique reagents, plasmids, or mouse lines. All unique/stable reagents used in this study are available from the lead contact with a completed Materials Transfer Agreement.

Data and code availability

- All data generated or analyzed during this study are included in this manuscript (and its supplementary information files). Raw human sequencing data including RNA-seq, DSP spatial sequencing, and scRNA-seq in this paper will be shared by the lead contact upon request. This paper also analyzes existing, publicly available data (deposited data of STAR Methods). Sequencing datasets generated in this article without human information are available publicly (deposited data of key resources table).
- scRNA-seq datasets were deposited into the Zenodo Database: https://zenodo.org/records/14249268.
- DSP spatial sequencing datasets were deposited into the Zenodo Database: https://zenodo.org/records/14249266.
- Bulk RNA-seq of CAF cell lines were deposited into the Zenodo Database: https://zenodo.org/records/14249260.
- This study did not generate any original code.
- Any additional information required to reanalyze the data reported in this paper is available from the lead contact upon request.

ACKNOWLEDGMENTS

We thank the patients and their families for their valuable and generous contributions to this study. This work was supported by the National Natural Science Foundation of China (82072564), Program of Shanghai Academic Research Leader (22XD142280), Shanghai Municipal Health Commission (2022XD029), National Multi-disciplinary Treatment Project for Major Diseases (2020NMDTP), Lian Yun Gang Shi Hui Lan Public Foundation (HL-HS2020-65), Yangtze River Delta joint sci-tech innovation and research projects (2023CSJZN0600), and Shanghai Chest Hospital Science and Technology Development Foundation (2021YNZYJ03).

AUTHOR CONTRIBUTIONS

Z.C. designed and performed experiments, analyzed data, and wrote the manuscript. Z.M. designed and performed bioinformatics analyses and wrote the manuscript. J.L. designed and performed *in vivo* experiments, analyzed data, and wrote the manuscript. Y.T. and L.L. collected patient samples and clinical information. A.W. and J.H. analyzed the data. J.W., J.S., and L.C. participated in discussions. S.L. and Z.L. conceived and supervised the study and wrote the manuscript. All authors read, reviewed, and revised the manuscript.

DECLARATION OF INTERESTS

The authors declare no competing interests.

STAR★METHODS

Detailed methods are provided in the online version of this paper and include the following:

- KEY RESOURCES TABLE
- EXPERIMENTAL MODEL AND STUDY PARTICIPANT DETAILS
  - Patient samples
  - Animals
  - Cell-lines and cell culture
- METHOD DETAILS
  - Quantitative reverse-transcription polymerase chain reaction (RT-qPCR)
  - Western blot assay
  - Flow cytometry
  - Multiplexed immunofluorescence assay
  - *In vivo* study
  - ELISA
  - Patient-derived CAFs 3D culture
  - RNA sequencing for patient-derived CAFs
  - Single-cell RNA sequencing
  - DSP spatial sequencing
  - Single-cell data analysis
  - Deconvolution based on GEPIA2021
  - Publicly-available bulk-RNA sequencing datasets analysis
  - Public spatial transcriptomics analysis
  - Biobank of patients TME
  - Construction of PDTF platform
  - Co-culture of CD4^{+} T cells with CAFs
- QUANTIFICATION AND STATISTICAL ANALYSIS

SUPPLEMENTAL INFORMATION

Supplemental information can be found online at https://doi.org/10.1016/j.xcrm.2025.102017.

Received: July 6, 2024
Revised: December 6, 2024
Accepted: February 14, 2025
Published: March 7, 2025

REFERENCES

1. Cascone, T., Leung, C.H., Weissferdt, A., Pataer, A., Carter, B.W., Godoy, M.C.B., Feldman, H., William, W.N., Xi, Y., Basu, S., et al. (2023). Neoadjuvant chemotherapy plus nivolumab with or without ipilimumab in operable non-small cell lung cancer: the phase 2 platform NEOSTAR trial. Nat. Med. *29*, 593–604. https://doi.org/10.1038/s41591-022-02189-0.
2. Versluis, J.M., Menzies, A.M., Sikorska, K., Rozeman, E.A., Saw, R.P.M., van Houdt, W.J., Eriksson, H., Klop, W.M.C., Ch'ng, S., van Thienen, J.V., et al. (2023). Survival update of neoadjuvant ipilimumab plus nivolumab in macroscopic stage III melanoma in the OpACIN and OpACIN-neo trials. Ann. Oncol. *34*, 420–430. https://doi.org/10.1016/j.annonc.2023.01.004.
3. Jiang, S., Liu, Y., Zheng, H., Zhang, L., Zhao, H., Sang, X., Xu, Y., and Lu, X. (2023). Evolutionary patterns and research frontiers in neoadjuvant immunotherapy: a bibliometric analysis. Int. J. Surg. *109*, 2774–2783. https://doi.org/10.1097/JS9.0000000000000492.
4. Passaro, A., Attili, I., and de Marinis, F. (2022). Neoadjuvant Chemotherapy Plus Immunotherapy in Early-Stage Resectable Non-Small-Cell Lung Cancer. J. Clin. Oncol. *40*, 2871–2877. https://doi.org/10.1200/JCO.22.00873.
5. Topalian, S.L., Taube, J.M., and Pardoll, D.M. (2020). Neoadjuvant checkpoint blockade for cancer immunotherapy. Science *367*, eaax0182. https://doi.org/10.1126/science.aax0182.
6. Provencio, M., Nadal, E., González-Larriba, J.L., Martínez-Martí, A., Bernabé, R., Bosch-Barrera, J., Casal-Rubio, J., Calvo, V., Insa, A., Ponce, S., et al. (2023). Perioperative Nivolumab and Chemotherapy in Stage III Non-Small-Cell Lung Cancer. N. Engl. J. Med. *389*, 504–513. https://doi.org/10.1056/NEJMoa2215530.
7. Shu, C.A., Gainor, J.F., Awad, M.M., Chiuzan, C., Grigg, C.M., Pabani, A., Garofano, R.F., Stoopler, M.B., Cheng, S.K., White, A., et al. (2020). Neoadjuvant atezolizumab and chemotherapy in patients with resectable non-small-cell lung cancer: an open-label, multicentre, single-arm, phase 2 trial. Lancet Oncol. *21*, 786–795. https://doi.org/10.1016/S1470-2045(20)30140-6.
8. Heymach, J.V., Harpole, D., Mitsudomi, T., Taube, J.M., Galffy, G., Hochmair, M., Winder, T., Zukov, R., Garbaos, G., Gao, S., et al. (2023). Perioperative Durvalumab for Resectable Non-Small-Cell Lung Cancer. N. Engl. J. Med. *389*, 1672–1684. https://doi.org/10.1056/NEJMoa2304875.
9. O'Brien, M., Paz-Ares, L., Marreaud, S., Dafni, U., Oselin, K., Havel, L., Esteban, E., Isla, D., Martinez-Marti, A., Faehling, M., et al. (2022). Pembrolizumab versus placebo as adjuvant therapy for completely resected stage IB-IIIA non-small-cell lung cancer (PEARLS/KEYNOTE-091): an interim analysis of a randomised, triple-blind, phase 3 trial. Lancet Oncol. *23*, 1274–1286. https://doi.org/10.1016/S1470-2045(22)00518-6.
10. Felip, E., Altorki, N., Zhou, C., Csőszi, T., Vynnychenko, I., Goloborodko, O., Luft, A., Akopov, A., Martinez-Marti, A., Kenmotsu, H., et al. (2021). Adjuvant atezolizumab after adjuvant chemotherapy in resected stage IB-IIIA non-small-cell lung cancer (IMpower010): a randomised, multicentre, open-label, phase 3 trial. Lancet *398*, 1344–1357. https://doi.org/10.1016/S0140-6736(21)02098-5.
11. Forde, P.M., Spicer, J., Lu, S., Provencio, M., Mitsudomi, T., Awad, M.M., Felip, E., Broderick, S.R., Brahmer, J.R., Swanson, S.J., et al. (2022). Neoadjuvant Nivolumab plus Chemotherapy in Resectable Lung Cancer. N. Engl. J. Med. *386*, 1973–1985. https://doi.org/10.1056/NEJMoa2202170.
12. Chaft, J.E., Oezkan, F., Kris, M.G., Bunn, P.A., Wistuba, I.I., Kwiatkowski, D.J., Owen, D.H., Tang, Y., Johnson, B.E., Lee, J.M., et al. (2022). Neoadjuvant atezolizumab for resectable non-small cell lung cancer: an open-label, single-arm phase II trial. Nat. Med. *28*, 2155–2161. https://doi.org/10.1038/s41591-022-01962-5.
13. Zhang, H., Yue, X., Chen, Z., Liu, C., Wu, W., Zhang, N., Liu, Z., Yang, L., Jiang, Q., Cheng, Q., et al. (2023). Define cancer-associated fibroblasts (CAFs) in the tumor microenvironment: new opportunities in cancer immunotherapy and advances in clinical trials. Mol. Cancer *22*, 159. https://doi.org/10.1186/s12943-023-01860-5.
14. Broz, M.T., Ko, E.Y., Ishaya, K., Xiao, J., De Simone, M., Hoi, X.P., Piras, R., Gala, B., Tessaro, F.H.G., Karlstaedt, A., et al. (2024). Metabolic targeting of cancer associated fibroblasts overcomes T-cell exclusion and chemoresistance in soft-tissue sarcomas. Nat. Commun. *15*, 2498. https://doi.org/10.1038/s41467-024-46504-4.
15. Tang, P.C.-T., Chung, J.Y.-F., Xue, V.W.-W., Xiao, J., Meng, X.-M., Huang, X.-R., Zhou, S., Chan, A.S.-W., Tsang, A.C.-M., Cheng, A.S.-L., et al. (2022). Smad3 Promotes Cancer-Associated Fibroblasts Generation via Macrophage-Myofibroblast Transition. Adv. Sci. *9*, e2101235. https://doi.org/10.1002/advs.202101235.
16. Zheng, S., Liang, J.-Y., Tang, Y., Xie, J., Zou, Y., Yang, A., Shao, N., Kuang, X., Ji, F., Liu, X., et al. (2023). Dissecting the role of cancer-associated fibroblast-derived biglycan as a potential therapeutic target in immunotherapy resistance: A tumor bulk and single-cell transcriptomic study. Clin. Transl. Med. *13*, e1189. https://doi.org/10.1002/ctm2.1189.
17. Huang, H., Wang, Z., Zhang, Y., Pradhan, R.N., Ganguly, D., Chandra, R., Murimwa, G., Wright, S., Gu, X., Maddipati, R., et al. (2022). Mesothelial cell-derived antigen-presenting cancer-associated fibroblasts induce expansion of regulatory T cells in pancreatic cancer. Cancer Cell *40*, 656–673.e7. https://doi.org/10.1016/j.ccell.2022.04.011.
18. Chen, L., Huang, H., Zheng, X., Li, Y., Chen, J., Tan, B., Liu, Y., Sun, R., Xu, B., Yang, M., et al. (2022). IL1R2 increases regulatory T cell population in the tumor microenvironment by enhancing MHC-II expression on cancer-associated fibroblasts. J. Immunother. Cancer *10*, e004585. https://doi.org/10.1136/jitc-2022-004585.
19. Li, J., Meng, Z., Cao, Z., Lu, W., Yang, Y., Li, Z., and Lu, S. (2024). ADGRE5-centered Tsurv model in T cells recognizes responders to neoadjuvant cancer immunotherapy. Front. Immunol. *15*, 1304183. https://doi.org/10.3389/fimmu.2024.1304183.
20. Meng, Z., Niu, X., Xia, L., Chen, Y., Wang, Z., Wang, H., Ji, P., Cui, W., Wang, Y., and Lu, S. (2023). A 3D Ex Vivo Tumor-Immune Coculture System Mimicking In Vivo Tumor Environmental Stress on CD8+ T Cells Exhaustion. Adv. Biol. *7*, e2200264. https://doi.org/10.1002/adbi.202200264.
21. Wang, Y., Du, J., Gao, Z., Sun, H., Mei, M., Wang, Y., Ren, Y., and Zhou, X. (2023). Evolving landscape of PD-L2: bring new light to checkpoint immunotherapy. Br. J. Cancer *128*, 1196–1207. https://doi.org/10.1038/s41416-022-02084-y.
22. Park, J.S., Gazzaniga, F.S., Wu, M., Luthens, A.K., Gillis, J., Zheng, W., LaFleur, M.W., Johnson, S.B., Morad, G., Park, E.M., et al. (2023). Targeting PD-L2–RGMb overcomes microbiome-related immunotherapy resistance. Nature *617*, 377–385. https://doi.org/10.1038/s41586-023-06026-3.
23. Du, Y., Shi, J., Wang, J., Xun, Z., Yu, Z., Sun, H., Bao, R., Zheng, J., Li, Z., and Ye, Y. (2024). Integration of Pan-Cancer Single-Cell and Spatial Transcriptomics Reveals Stromal Cell Features and Therapeutic Targets in Tumor Microenvironment. Cancer Res. *84*, 192–210. https://doi.org/10.1158/0008-5472.CAN-23-1418.
24. Xiao, Z., Todd, L., Huang, L., Noguera-Ortega, E., Lu, Z., Huang, L., Kopp, M., Li, Y., Pattada, N., Zhong, W., et al. (2023). Desmoplastic stroma restricts T cell extravasation and mediates immune exclusion and immunosuppression in solid tumors. Nat. Commun. *14*, 5110. https://doi.org/10.1038/s41467-023-40850-5.

25. Jung, H., Kim, H.S., Kim, J.Y., Sun, J.-M., Ahn, J.S., Ahn, M.-J., Park, K., Esteller, M., Lee, S.-H., and Choi, J.K. (2019). DNA methylation loss promotes immune evasion of tumours with high mutation and copy number load. Nat. Commun. *10*, 4278. https://doi.org/10.1038/s41467-019-12159-9.

26. Hu, J., Zhang, L., Xia, H., Yan, Y., Zhu, X., Sun, F., Sun, L., Li, S., Li, D., Wang, J., et al. (2023). Tumor microenvironment remodeling after neoadjuvant immunotherapy in non-small cell lung cancer revealed by single-cell RNA sequencing. Genome Med. *15*, 14. https://doi.org/10.1186/s13073-023-01164-9.

27. Kerdidani, D., Aerakis, E., Verrou, K.-M., Angelidis, I., Douka, K., Maniou, M.-A., Stamoulis, P., Goudevenou, K., Prados, A., Tzaferis, C., et al. (2022). Lung tumor MHCII immunity depends on in situ antigen presentation by fibroblasts. J. Exp. Med. *219*, e20210815. https://doi.org/10.1084/jem.20210815.

28. Voabil, P., de Bruijn, M., Roelofsen, L.M., Hendriks, S.H., Brokamp, S., van den Braber, M., Broeks, A., Sanders, J., Herzig, P., Zippelius, A., et al. (2021). An ex vivo tumor fragment platform to dissect response to PD-1 blockade in cancer. Nat. Med. *27*, 1250–1261. https://doi.org/10.1038/s41591-021-01398-3.

29. Elyada, E., Bolisetty, M., Laise, P., Flynn, W.F., Courtois, E.T., Burkhart, R.A., Teinor, J.A., Belleau, P., Biffi, G., Lucito, M.S., et al. (2019). Cross-Species Single-Cell Analysis of Pancreatic Ductal Adenocarcinoma Reveals Antigen-Presenting Cancer-Associated Fibroblasts. Cancer Discov. *9*, 1102–1123. https://doi.org/10.1158/2159-8290.CD-19-0094.

30. Bonnin, E., Rodrigo Riestra, M., Marziali, F., Mena Osuna, R., Denizeau, J., Maurin, M., Saez, J.J., Jouve, M., Bonté, P.-E., Richer, W., et al. (2024). CD74 supports accumulation and function of regulatory T cells in tumors. Nat. Commun. *15*, 3749. https://doi.org/10.1038/s41467-024-47981-3.

31. Shevyrev, D., and Tereshchenko, V. (2019). Treg Heterogeneity, Function, and Homeostasis. Front. Immunol. *10*, 3100. https://doi.org/10.3389/fimmu.2019.03100.

32. Freuchet, A., Roy, P., Armstrong, S.S., Oliaeimotlagh, M., Kumar, S., Orecchioni, M., Ali, A.J., Khan, A., Makings, J., Lyu, Q., et al. (2023). Identification of human exTreg cells as CD16+ CD56+ cytotoxic CD4+ T cells. Nat. Immunol. *24*, 1748–1761. https://doi.org/10.1038/s41590-023-01589-9.

33. Mair, F., Erickson, J.R., Frutoso, M., Konecny, A.J., Greene, E., Voillet, V., Maurice, N.J., Rongvaux, A., Dixon, D., Barber, B., et al. (2022). Extricating human tumour immune alterations from tissue inflammation. Nature *605*, 728–735. https://doi.org/10.1038/s41586-022-04718-w.

34. Itahashi, K., Irie, T., Yuda, J., Kumagai, S., Tanegashima, T., Lin, Y.-T., Watanabe, S., Goto, Y., Suzuki, J., Aokage, K., et al. (2022). BATF epigenetically and transcriptionally controls the activation program of regulatory T cells in human tumors. Sci. Immunol. *7*, eabk0957. https://doi.org/10.1126/sciimmunol.abk0957.

35. Mensink, M., Verleng, L.J., Schrama, E., Janssen, G.M., Tjokrodirijo, R.T., van Veelen, P.A., Jiang, Q., Pascutti, M.F., van der Hoorn, M.L., Eikmans, M., et al. (2024). Tregs from human blood differentiate into nonlymphoid tissue–resident effector cells upon TNFR2 costimulation. JCI Insight *9*, e172942. https://doi.org/10.1172/jci.insight.172942.

36. Ghosh, S., Roy-Chowdhuri, S., Kang, K., Im, S.-H., and Rudra, D. (2018). The transcription factor Foxp1 preserves integrity of an active Foxp3 locus in extrathymic Treg cells. Nat. Commun. *9*, 4473. https://doi.org/10.1038/s41467-018-07018-y.

37. Konopacki, C., Pritykin, Y., Rubtsov, Y., Leslie, C.S., and Rudensky, A.Y. (2019). Transcription factor Foxp1 regulates Foxp3 chromatin binding and coordinates regulatory T cell function. Nat. Immunol. *20*, 232–242. https://doi.org/10.1038/s41590-018-0291-z.

38. Ren, J., Han, L., Tang, J., Liu, Y., Deng, X., Liu, Q., Hao, P., Feng, X., Li, B., Hu, H., and Wang, H. (2019). Foxp1 is critical for the maintenance of regulatory T-cell homeostasis and suppressive function. PLoS Biol. *17*, e3000270. https://doi.org/10.1371/journal.pbio.3000270.

39. De Zuani, M., Xue, H., Park, J.S., Dentro, S.C., Seferbekova, Z., Tessier, J., Curras-Alonso, S., Hadjipanayis, A., Athanasiadis, E.I., Gerstung, M., et al. (2024). Single-cell and spatial transcriptomics analysis of non-small cell lung cancer. Nat. Commun. *15*, 4388. https://doi.org/10.1038/s41467-024-48700-8.

40. Sudmeier, L.J., Hoang, K.B., Nduom, E.K., Wieland, A., Neill, S.G., Schniederjan, M.J., Ramalingam, S.S., Olson, J.J., Ahmed, R., and Hudson, W.H. (2022). Distinct phenotypic states and spatial distribution of CD8+ T cell clonotypes in human brain metastases. Cell Rep. Med. *3*, 100620. https://doi.org/10.1016/j.xcrm.2022.100620.

41. Cheng, H.-Y., Hsieh, C.-H., Lin, P.-H., Chen, Y.-T., Hsu, D.S.-S., Tai, S.-K., Chu, P.-Y., and Yang, M.-H. (2022). Snail-regulated exosomal microRNA-21 suppresses NLRP3 inflammasome activity to enhance cisplatin resistance. J. Immunother. Cancer *10*, e004832. https://doi.org/10.1136/jitc-2022-004832.

42. Wu, Y., Yang, S., Ma, J., Chen, Z., Song, G., Rao, D., Cheng, Y., Huang, S., Liu, Y., Jiang, S., et al. (2022). Spatiotemporal Immune Landscape of Colorectal Cancer Liver Metastasis at Single-Cell Level. Cancer Discov. *12*, 134–153. https://doi.org/10.1158/2159-8290.CD-21-0316.

43. Obradovic, A., Chowdhury, N., Haake, S.M., Ager, C., Wang, V., Vlahos, L., Guo, X.V., Aggen, D.H., Rathmell, W.K., Jonasch, E., et al. (2021). Single-cell protein activity analysis identifies recurrence-associated renal tumor macrophages. Cell *184*, 2988–3005.e16. https://doi.org/10.1016/j.cell.2021.04.038.

44. Hurrell, B.P., Helou, D.G., Howard, E., Painter, J.D., Shafiei-Jahani, P., Sharpe, A.H., and Akbari, O. (2022). PD-L2 controls peripherally induced regulatory T cells by maintaining metabolic activity and Foxp3 stability. Nat. Commun. *13*, 5118. https://doi.org/10.1038/s41467-022-32899-5.

45. Garcia-Diaz, A., Shin, D.S., Moreno, B.H., Saco, J., Escuin-Ordinas, H., Rodriguez, G.A., Zaretsky, J.M., Sun, L., Hugo, W., Wang, X., et al. (2017). Interferon Receptor Signaling Pathways Regulating PD-L1 and PD-L2 Expression. Cell Rep. *19*, 1189–1201. https://doi.org/10.1016/j.celrep.2017.04.031.

46. Lazear, H.M., Schoggins, J.W., and Diamond, M.S. (2019). Shared and Distinct Functions of Type I and Type III Interferons. Immunity *50*, 907–923. https://doi.org/10.1016/j.immuni.2019.03.025.

47. Cao, X., Liang, Y., Hu, Z., Li, H., Yang, J., Hsu, E.J., Zhu, J., Zhou, J., and Fu, Y.-X. (2021). Next generation of tumor-activating type I IFN enhances anti-tumor immune responses to overcome therapy resistance. Nat. Commun. *12*, 5866. https://doi.org/10.1038/s41467-021-26112-2.

48. Liu, Y.-T., and Sun, Z.-J. (2021). Turning cold tumors into hot tumors by improving T-cell infiltration. Theranostics *11*, 5365–5386. https://doi.org/10.7150/thno.58390.

49. Yu, M., Peng, Z., Qin, M., Liu, Y., Wang, J., Zhang, C., Lin, J., Dong, T., Wang, L., Li, S., et al. (2021). Interferon-γ induces tumor resistance to anti-PD-1 immunotherapy by promoting YAP phase separation. Mol. Cell *81*, 1216–1230.e9. https://doi.org/10.1016/j.molcel.2021.01.010.

50. Memon, D., Schoenfeld, A.J., Ye, D., Fromm, G., Rizvi, H., Zhang, X., Keddar, M.R., Mathew, D., Yoo, K.J., Qiu, J., et al. (2024). Clinical and molecular features of acquired resistance to immunotherapy in non-small cell lung cancer. Cancer Cell *42*, 209–224.e9. https://doi.org/10.1016/j.ccell.2023.12.013.

51. Kieffer, Y., Hocine, H.R., Gentric, G., Pelon, F., Bernard, C., Bourachot, B., Lameiras, S., Albergante, L., Bonneau, C., Guyard, A., et al. (2020). Single-Cell Analysis Reveals Fibroblast Clusters Linked to Immunotherapy Resistance in Cancer. Cancer Discov. *10*, 1330–1351. https://doi.org/10.1158/2159-8290.CD-19-1384.

52. Lakins, M.A., Ghorani, E., Munir, H., Martins, C.P., and Shields, J.D. (2018). Cancer-associated fibroblasts induce antigen-specific deletion of CD8+ T Cells to protect tumour cells. Nat. Commun. *9*, 948. https://doi.org/10.1038/s41467-018-03347-0.

53. Sekiya, T., and Takaki, S. (2019). RGMB enhances the suppressive activity of the monomeric secreted form of CTLA-4. Sci. Rep. *9*, 6984. https://doi.org/10.1038/s41598-019-43068-y.

54. Mathew, D., Marmarelis, M.E., Foley, C., Bauml, J.M., Ye, D., Ghinnagow, R., Ngiow, S.F., Klapholz, M., Jun, S., Zhang, Z., et al. (2024). Combined JAK inhibition and PD-1 immunotherapy for non–small cell lung cancer patients. Science *384*, eadf1329. https://doi.org/10.1126/science.adf1329.

55. Zak, J., Pratumchai, I., Marro, B.S., Marquardt, K.L., Zavareh, R.B., Lairson, L.L., Oldstone, M.B.A., Varner, J.A., Hegerova, L., Cao, Q., et al. (2024). JAK inhibition enhances checkpoint blockade immunotherapy in patients with Hodgkin lymphoma. Science *384*, eade8520. https://doi.org/10.1126/science.ade8520.

56. Chen, Y., Wang, D., Li, Y., Qi, L., Si, W., Bo, Y., Chen, X., Ye, Z., Fan, H., Liu, B., et al. (2024). Spatiotemporal single-cell analysis decodes cellular dynamics underlying different responses to immunotherapy in colorectal cancer. Cancer Cell *42*, 1268–1285.e7. https://doi.org/10.1016/j.ccell.2024.06.009.

57. Hao, Y., Stuart, T., Kowalski, M.H., Choudhary, S., Hoffman, P., Hartman, A., Srivastava, A., Molla, G., Madad, S., Fernandez-Granda, C., and Satija, R. (2024). Dictionary learning for integrative, multimodal and scalable single-cell analysis. Nat. Biotechnol. *42*, 293–304. https://doi.org/10.1038/s41587-023-01767-y.

58. Li, C., Tang, Z., Zhang, W., Ye, Z., and Liu, F. (2021). GEPIA2021: integrating multiple deconvolution-based analysis into GEPIA. Nucleic Acids Res. *49*, W242–W246. https://doi.org/10.1093/nar/gkab418.

59. Shi, J., Wei, X., Xun, Z., Ding, X., Liu, Y., Liu, L., and Ye, Y. (2024). The Web-Based Portal SpatialTME Integrates Histological Images with Single-Cell and Spatial Transcriptomics to Explore the Tumor Microenvironment. Cancer Res. *84*, 1210–1220. https://doi.org/10.1158/0008-5472.CAN-23-2650.

STAR★METHODS

KEY RESOURCES TABLE

REAGENT or RESOURCE	SOURCE	IDENTIFIER
Antibodies		
Rabbit anti-PDCD1LG2 Polyclonal Antibody	Absin Bioscience	Cat# abs132940; RRID: AB_3665446
Anti-mouse IgG, HRP-linked Antibody	CST	Cat# 7076; RRID: AB_330924
Rabbit anti-FOXP1 Recombinant Monoclonal Antibody(R053)	Absin Bioscience	Cat# abs171707; RRID: AB_3665447
Donkey anti-Goat IgG-AlexaFluor 647	Absin Bioscience	Cat# abs20027; RRID: AB_3665449
Rabbit anti-IFI27 Polyclonal Antibody	Absin Bioscience	Cat# abs138509; RRID: AB_3665451
Anti-IFNg Reference Antibody(Emapalumab)	Absin Bioscience	Cat# abs172010; RRID: AB_3665459
Rabbit anti-IFI6 Polyclonal Antibody	Absin Bioscience	Cat# abs139635; RRID: AB_3665461
Rabbit anti-JAK1 Polyclonal Antibody	Absin Bioscience	Cat# abs131173; RRID: AB_3665464
Rabbit anti-Phospho-JAK1(Tyr1022) Polyclonal Antibody	Absin Bioscience	Cat# abs130626; RRID: AB_3665465
Rabbit anti-STAT1 Polyclonal Antibody	Absin Bioscience	Cat# abs131817; RRID: AB_3665467
Rabbit anti-Phospho-STAT1(Tyr701)	Absin Bioscience	Cat# abs130925; RRID: AB_3665468
HLA-DR Rabbit Monoclonal Antibody	Beyotime Biotechnology	Cat# AF2065; RRID: AB_3665511
JAK2 Rabbit Monoclonal Antibody	Beyotime Biotechnology	Cat# AF1489; RRID: AB_3665512
Phospho-Jak2 (Tyr1007/1008) Rabbit Polyclonal Antibody	Beyotime Biotechnology	Cat# AF5854; RRID: AB_3665514
IFNGR1 Rabbit Polyclonal Antibody	Beyotime Biotechnology	Cat# AF7176; RRID: AB_3665513
STAT3 Rabbit Polyclonal Antibody (KO Validated)	Beyotime Biotechnology	Cat# AF5315; RRID: AB_3665515
Phospho-STAT3 (Tyr705) Rabbit Polyclonal Antibody	Beyotime Biotechnology	Cat# AF5941; RRID: AB_3665525
Anti-alpha smooth muscle Actin antibody [1A4]	Abcam	Cat# ab7817; RRID: AB_262054
GAPDH Antibody	Proteintech	Cat# CL650-60004; RRID: AB_2920461
Zombie UV™ Fixable Viability	Biolegend	Cat# 423107; RRID: AB_3676450
BD Horizon™ Fixable Viability Stain 510	BD Biosciences	Cat# 564406; RRID:AB_2869572
BD Horizon™ Fixable Viability Stain 440UV	BD Biosciences	Cat# 566332; RRID:AB_2869748
PE/Cyanine7 anti-mouse CD45	Biolegend	Cat# 103113; RRID: AB_312978
APC/Cyanine7 anti-mouse CD45	Biolegend	Cat# 103115; RRID: AB_312980
APC anti-human CD45	Biolegend	Cat# 304011; RRID: AB_314399
BD Pharmingen™ FITC Mouse Anti-Human CD45	BD Biosciences	Cat# 560976; RRID: AB_10563935
Brilliant Violet 510(TM) anti-mouse CD3	Biolegend	Cat# 100234; RRID: AB_2562555
CD4 Monoclonal Antibody (RM4-5), Alexa Fluor™ 700	Thermo Fisher Scientific	Cat# 56-0042-82; RRID: AB_494000
Rat Anti-CD8a Monoclonal Antibody, Phycoerythrin Conjugated, Clone 53–6.7	BD Biosciences	Cat# 553032; RRID: AB_394570
Mouse Anti-CD25 Monoclonal Antibody, FITC Conjugated, Clone M-A251	BD Biosciences	Cat# 555431; RRID: AB_395825
CD25 Monoclonal Antibody (PC61.5), PE-Cyanine7	Thermo Fisher Scientific	Cat# 25-0251-81; RRID: AB_469607
APC anti-mouse CD31	Biolegend	Cat# 102409; RRID: AB_312904
FITC anti-human CD31	Biolegend	Cat# 303103; RRID: AB_314329
BD Horizon™ BV421 Mouse Anti-Human CD274	BD Biosciences	Cat# 563738; RRID: AB_2738396
BD Pharmingen™ Alexa Fluor® 647 Rat Anti-Mouse CD279 (PD-1)	BD Biosciences	Cat# 566715; RRID: AB_2739769
BD Pharmingen™ APC Rat Anti-Mouse CD326	BD Biosciences	Cat# 563478; RRID: AB_2738234

(*Continued on next page*)

Continued

REAGENT or RESOURCE	SOURCE	IDENTIFIER
PerCP/Cyanine5.5 anti-human CD326	Biolegend	Cat# 324213; RRID: AB_893474
FOXP3 Monoclonal Antibody (FJK-16s), APC	Thermo Fisher Scientific	Cat# 17-5773-82; RRID: AB_469457
Brilliant Violet 421(TM) anti-human FOXP3	Biolegend	Cat# 320123; RRID: AB_2561338
APC/Fire™ 750 anti-mouse IFN-γ	Biolegend	Cat# 505859; RRID: AB_2814431
Alexa Fluor(R) 488 anti-Hsp70	Biolegend	Cat# 648003; RRID: AB_2119539
PE/Cyanine7 anti-human HLA-DR	Biolegend	Cat# 307615; RRID:AB_493589
APC/Cyanine7 anti-human Podoplanin	Biolegend	Cat# 337029; RRID: AB_2750289
FITC anti-mouse Podoplanin	Biolegend	Cat# 127415; RRID: AB_2629801
FITC anti-human/mouse Granzyme B	Biolegend	Cat# 515403; RRID: AB_2114575
Brilliant Violet 605™ anti-mouse Ly-6C	Biolegend	Cat# 128035; RRID: AB_2562352
PerCP/Cyanine5.5 anti-mouse I-A/I-E	Biolegend	Cat# 107625; RRID: AB_2191072
Mouse RGM-B Antibody	R&D Systems	Cat# AF3597; RRID: AB_2179484
Donkey anti-Rabbit IgG (H + L) ReadyProbes Secondary Antibody, Alexa Fluor™ 488	Thermo Fisher Scientific	Cat# R37118; RRID: AB_2556546
Goat anti-Rabbit IgG (H + L) Cross-Adsorbed Secondary Antibody, Alexa Fluor™ 594	Thermo Fisher Scientific	Cat# A-11012; RRID: AB_2534079
CD74 (D5N3I) XP® Rabbit mAb	CST	Cat# 77274; RRID: AB_2799893
FoxP3 (D2W8E™) (IHC Specific)	CST	Cat# 98377; RRID: AB_2747370
Anti-CD74 Rabbit pAb	Servicebio	Cat# GB115427; RRID: AB_3665805
Anti -Collagen I Rabbit pAb	Servicebio	Cat# GB114197; RRID: AB_3665662
Anti-Collagen III Rabbit pAb	Servicebio	Cat# GB111629; RRID: AB_3073715
Anti-PD-L1 Rabbit pAb	Servicebio	GB115704; RRID: AB_3665669
Anti-alpha smooth muscle Actin Rabbit pAb	Servicebio	Cat# GB111364; RRID: AB_2910228
InVivoPlus anti-mouse PD-1 (CD279)	BioXcell	Cat# BE0146; RRID: AB_10949053
Anti-Mouse CD273 (PD-L2) - Purified *In vivo*	Leinco Technologies	Cat# P379; RRID: AB_2737559
InVivoMAb anti-mouse RGMb	BioXcell	Cat# BE0400; RRID: AB_3665663
InVivoMAb rat IgG2b isotype control	BioXcell	Cat# BE0090; RRID: AB_1107780
InVivoMAb rat IgG2a isotype control	BioXcell	Cat# BE0089; RRID: AB_1107769
InVivoMAb anti-human/monkey MHC class II (HLA-DR)	BioXcell	Cat# BE0306; RRID: AB_2736986
Nivolumab	Bristol Myers Squibb	NA
Anti-β-Gal-hIgG4 (S228P)	InvivoGen	Cat# bgal-mab114; RRID: AB_3665664
Biological samples		
Human NSCLC biopsy tissue	Shanghai Chest Hospital, Shanghai Jiao Tong University School of Medicine	N/A
Human NSCLC surgery tissue	Shanghai Chest Hospital, Shanghai Jiao Tong University School of Medicine	N/A
Chemicals, peptides, and recombinant proteins		
TRIzol	Invitrogen	Cat# 15596018
RIPA Buffer	Thermo Fisher Scientific	Cat# 89901
Protease inhibitor cocktail	TargetMol	Cat# C0001
Phosphatase inhibitor cocktail	TargetMol	Cat# C0003
Bovine Serum Albumin	Sangon	Cat# A600332-0100
Cell Activation Cocktail (with Brefeldin A)	Biolegend	Cat# 423303
Cell Activation Cocktail (without Brefeldin A)	Biolegend	Cat# 423301
Cyto-Fast™ Fix/Perm Buffer Set	Biolegend	Cat# 426803
True-Nuclear™ Transcription Factor Buffer Set	Biolegend	Cat# 424401

(*Continued on next page*)

Continued

REAGENT or RESOURCE	SOURCE	IDENTIFIER
GelMA-PEO phase-separation hydrogel	Engineering For Life	Cat# EFL-GM-PR-002
Dynabeads™ Human T-Activator CD3/CD28	Thermo Fisher Scientific	Cat# 11161D
ACCUTASE™ Cell Detachment Solution	Stemcell	Cat# 07920
ImmunoCult™ Human CD3/CD28 T cell Activator	Stemcell	Cat# 10971
Human IL-2	Peprotech	Cat# 200-02
Human TGF-β	Peprotech	Cat# 100-21
Retinoic acid	MedChemExpress	Cat# HY-14649
Rapamycin	MedChemExpress	Cat# 53123-88-9
Recombinant Human IFN-β	Peprotech	Cat# 300-02BC
Recombinant Human IFN-α (2a)	Peprotech	Cat# 300-02AA
Recombinant Human IFN-γ	Peprotech	Cat# 300-02
Anifrolumab	selleck	Cat# A2460
IFN alpha-IFNAR-IN-1 hydrochloride	selleck	Cat# E2982
Fludarabine	selleck	Cat# S1491
Ruxolitinib	Beyotime Biotechnology	Cat# SD4740
NSC 74859	Beyotime Biotechnology	Cat# SD4794
Recombinant Human IFN-λ1	Peprotech	Cat# 300-02L
Matrigel® Basement Membrane Matrix Growth Factor Reduced	Corning	Cat# 356231
Matrigel® Basement Membrane Matrix	Corning	Cat# 354234
PrimeScriptTM RT reagent Kit	Takara	Cat# RR037B
TB GreenTM Premix Ex TaqTM II	Takara	Cat# RR82WR
RPMI 1640 Medium	Thermo Fisher Scientific	Cat# 11875093
Fetal Bovine Serum	Gibco	Cat# 10099141
Penicillin-Streptomycin	Thermo Fisher Scientific	Cat# 15140122
Dulbecco's Modified Eagle Medium (DMEM) without D-Glucose	Thermo Fisher Scientific	Cat# 11966025
DAPI solution	Solarbio	Cat# 28718-90-3
Critical commercial assays		
BCA Protein Assay Kit	Takara	Cat# T9300A
Multiple fluorescent immunohistochemical staining kit	Absin	Cat# abs50030
IFNγ enzyme-linked immunosorbent assay (ELISA) kit	Servicebio	Cat# GEH0006
Human Tumor Dissociated Kit	Miltenyi Biotec	Cat# 130-095-929
Mouse Tumor Dissociated Kit	Miltenyi Biotec	Cat# 130-096-730
CD45 (TIL) Microbeads, human	Miltenyi Biotec	Cat# 130-118-780
MojoSort™ Human CD4 Naive T cell Isolation Kit	Biolegend	Cat# 480042
Deposited data		
Bulk RNA-sequencing dataset	This paper	Zenodo: https://zenodo.org/records/14249260
scRNA-sequencing dataset	This paper	Zenodo: https://zenodo.org/records/14249268
DSP spatial-sequencing dataset	This paper	Zenodo: https://zenodo.org/records/14249266
Human NSCLC patients-scRNA-seq	Hu et al., 2023[26]	GEO: GSE207422
Human brain metastases patients-Spatial transcriptomics (10x Visium)	Sudmeier et al., 2021[40]	GEO: GSE179572
Human HNSCC patients-Spatial transcriptomics (10x Visium)	Cheng et al., 2022[41]	GEO: GSE181300
Human NSCLC patients-Spatial transcriptomics (10x Visium)	De Zuani et al., 2024[39]	EMBL-EBI: https://www.ebi.ac.uk/biostudies/arrayexpress/studies/E-MTAB-13530
Infiltrating T cells from mouse tumor-bulk ATAC-seq	Itahashi et al., 2022[34]	GEO: GSE211062
Treg from human bulk-RNA	Mensink et al., 2024[35]	GEO: GSE253540

(*Continued on next page*)

Continued

REAGENT or RESOURCE	SOURCE	IDENTIFIER
T cell subsets from human PBMC-bulk-RNA	Itahashi et al., 2022[34]	GEO: GSE211044
RNA-seq for 27 NSCLC patients treated with anti-PD-1/PD-L1	Jung et al., 2019[25]	GEO: GSE135222
Experimental models: Cell lines		
Human: A549	SIBCB (Shanghai, China)	Cat# SCSP-503
Human: HFL1	SIBCB (Shanghai, China)	Cat# SCSP-5049
Mouse: LLC	SIBCB (Shanghai, China)	Cat# SCSP-5252
Mouse: MF	iCell Bioscience (Shanghai, China)	Cat# iCell-0033a
Mouse: KP	Gift from Dr. Deng	N/A
Mouse: SJT1601	Gift from Prof. Deng	N/A
Experimental models: Organisms/strains		
Mouse: C57BL/6J	Shanghai Model Organisms (Shanghai, China)	N/A
Oligonucleotides		
RT-qPCR primer sequences, see Table S7	This paper	N/A
siRNA targeting sequence for IFI6: GCAGCGUCGUCAUAGGUAATT UUACCUAUGACGACGCUGCTT	Obio Technology (Shanghai, China)	N/A
siRNA targeting sequence for IFI27: GGCCAGGAUUGCUACAGUUTT AACUGUAGCAAUCCUGGCCTT	Obio Technology (Shanghai, China)	N/A
Negative control siRNA sequence: UUCUCCGAACGUGUCACGUTT ACGUGACACGUUCGGAGAATT	Obio Technology (Shanghai, China)	N/A
shRNA targeting sequence for Ifngr: GCCAGAGTTAAAGCTAAGGTT	Genepharma (Shanghai, China)	N/A
Software and algorithms		
ImageJ	National Institutes of Health	https://imagej.net/ij/
SlideViewer	The Digital Pathology Company	https://www.3dhistech.com/research/software-downloads/
BioRender	NA	https://biorender.com/
GraphPad Prism version 9.5.0	GraphPad Software	https://www.graphpad.com/
Gepia2	Zefang Tang, Tianxiang Chen, Chenwei Li and Boxi Kang of Zhang Lab, Peking University.	http://gepia2.cancer-pku.cn
FlowJo version 10.8.1	FlowJo	https://www.flowjo.com
R version 4.4.1	The R Foundation	https://www.r-project.org/

EXPERIMENTAL MODEL AND STUDY PARTICIPANT DETAILS

Patient samples

Patient samples were collected from Shanghai Chest Hospital, Shanghai, China. Patients were considered eligible for inclusion in this study if they met the following criteria: aged 20–75 years; clinical stage IIA to IIIB disease based on the American Joint Committee on Cancer (AJCC) Lung Cancer Staging, 8th edition (2017); an Eastern Cooperative Oncology Group performance-status score of 0 or 1; histologically confirmed NSCLC; and no previous anticancer therapy. Patients with a pathological type of small cell lung cancer or for whom tissue samples for scRNA-seq or DSP-seq were not available were excluded. Written informed consent was obtained from all patients participated in this study and the use of patients' specimens was conducted with the approval of the Ethics Committee of Shanghai Chest Hospital [Approval ID: KS1971].

Animals

C57BL/6J mice, aged 6 and 8 weeks, were purchased from Shanghai Model Organisms. All mice were housed in a specific pathogen-free Animal Center of Shanghai Chest Hospital with 24 h access to food and water. The temperature of the housing environment

ranged from 24°C to 26°C and the humidity ranged from 50% to 70%. All animal procedures were received approval from the Animal Ethics Committee of Shanghai Chest Hospital [Approval ID: KS23014-(A)].

Cell-lines and cell culture

Primary CAFs were isolated from lung tumor samples obtained from patients and the details see method (Patient-derived CAFs 3D culture). The lung cancer cell-lines A549 and LLC, and human fibroblast cell-line (HFL1) were purchased from the Shanghai Institute for Biological Sciences Chinese Academy of Sciences (Shanghai, China). The C57BL/6J fibroblast cell-line (MF) were obtained from iCell Bioscience (Shanghai, China). SJT1601 and KP cell on a C57BL/6 background were kindly provided by Prof. Deng from Shanghai Jiaotong University School of Medicine. All the mentioned cell-lines were cultured in Dulbecco's Modified Eagle Medium (DMEM, Thermo Fisher Scientific) with 10% fetal bovine serum (FBS, Gibco) and 1% penicillin/streptomycin (P/S, Thermo Fisher Scientific) at 37°C with 5% CO2 atmosphere.

METHOD DETAILS

Quantitative reverse-transcription polymerase chain reaction (RT-qPCR)

Organoids ($EPCAM^+CD45^-$), TILs ($CD45^+EPCAM^-$) and CAFs ($CD45^-EPCAM^-PDPN^+$) were sorted (detailed in STAR Methods: biobank of patients TME) and then RT-qPCR was conducted upon them respectively (related to Figure 5G). In other situations, RT-qPCR was conducted as needed. Total RNA was isolated from cells using TRIzol reagent (Invitrogen). cDNA was synthesized from 500ng of total RNA using a reverse transcription kit (Takara). RT-qPCR was using SYBR Green PCR Master Mix (Takara) and monitored in real-time using an ABI 7500 System (Applied Biosystems). Relative gene expression levels were analyzed using the $2^{-\Delta\Delta Ct}$ method. The primers used for RT-qPCR are listed in Table S7.

Western blot assay

Cells were lysed on ice in RIPA buffer (Thermo Fisher Scientific) containing protease and phosphatase inhibitor cocktail (TargetMol) for 30 min. Lysates were subsequently centrifuged at 15000 x g and protein concentration was determined using the BCA kit (Takara). Cell lysates were subjected to 10% sodium dodecyl sulfate-polyacrylamide gel electrophoresis (SDS-PAGE) and thereafter transferred onto polyvinylidene difluoride membranes (Millipore). The membranes were blocked using 5% Bovine Serum Albumin (BSA) at room temperature (RT) for 1 h and then incubated with primary antibodies overnight at 4°C. After incubation with appropriate HRP-linked secondary antibodies (Cell Signaling) for 1 h at RT, chemiluminescence was detected using an Amersham Imager 6000 (GE) with enhanced chemiluminescence (ECL) solution (Thermo Fisher Scientific).

Flow cytometry

For 2D or 3D culture, the flow cytometry experiments were conducted at passage4; for PDTFs, it was conducted on day2 since the establishment. For the analysis on surface markers, cells were resuspended in FACS buffer (PBS containing 2% FBS) and stained with fluorescent-conjugated antibodies at 1:400 dilution on ice for 30 min in the dark. Stained cells were washed once with FACS buffer and fixed in PBS containing 1% paraformaldehyde. For intracellular cytokine detection, cells were stimulated with Cell Activation Cocktail (Biolegend) for 4 h. After the stimulation, surface antigen staining was performed in FACS buffer, followed by intracellular staining using the Cyto-Fast Fix/Perm Buffer Set (Biolegend) according to the manufacturer's protocol. For intracellular transcriptional factor staining, cells were harvested and washed with FACS buffer for twice. Cells were firstly labeled with surface markers before permeabilized and stained with True-Nuclear Transcription Factor Buffer Set (Biolegend). Stained cells were washed twice with FACS buffer and acquired on a BD FACSFortessa (BD Bioscience). Data were analyzed with FlowJo (v10.8.1). To sort apCAFs or non-apCAFs, single-cell suspension from tissues were freshly stained with Fixable Viability Dye, EpCAM, CD45, CD31, PDPN, I-A/I-E for 30 min at 4°C in the dark. Cells were then washed and resuspended in FACS buffer. The suspension was sorted on a BD FACS AriaIII (BD Bioscience) gated on live, $EpCAM^-$, $CD45^-$, $CD31^-$, $PDPN^+$, $I\text{-}A/I\text{-}E^+$ for apCAFs and live, $EpCAM^-$, $CD45^-$, $CD31^-$, $PDPN^+$, $I\text{-}A/I\text{-}E^-$ for non-apCAFs. The flow cytometry staining panel was listed in Table S6, and the gating strategy was presented in Figure S14.

Multiplexed immunofluorescence assay

Fresh tumor tissues were fixed in 4% polyformaldehyde for more than 24 h and then kept in 70% ethanol at 4°C until processed into paraffin blocks. 5–10 μM sections were sliced on clean slides and performed immunofluorescence assay. Briefly, after the procedures of deparaffinization, rehydration, antigen retrieval, PBS with 3% BSA was added to the tissues to block non-specific binding at RT for 1 h. After blocking, slides were incubated with primary antibodies overnight at 4°C in a wet box, followed by horseradish peroxidase-conjugated secondary antibody incubation and tyramide signal amplification by using a multiple fluorescent immunohistochemical staining kit (Absin, Shanghai, China). The slides were microwave heat-treated after each TSA operation. Nuclei were stained with DAPI after all tumor antigens had been labeled. For immunochemistry staining for cells, 2% polyformaldehyde was using to fix the cells, following a 10 min permeabilization step. Then the cells were blocked for 30 min, and stained with primary antibodies at 4°C overnight. On the next day, fluorescently labeled secondary antibodies were incubated at RT for 1 h. To obtain multispectral images, the stained slides were scanned using the PerkinElmer Vectra 3 system (PerkinElmer) and analyzed by using ImageJ software.

In vivo study

C57BL/6J mice, aged 6 and 8 weeks, were housed under standard special pathogen-free conditions. All animal procedures were received approval from the Animal Ethics Committee of Shanghai Chest Hospital. For orthotopic lung tumor models, we anesthetized the mice using inhalation anesthesia with isoflurane. A 1 cm incision was made along the upper edge of the rib cage to exposure the lung tissue. We then generated mouse tumor by injection of 5×10^5 Lewis lung cancer (LLC) cells resuspended in 50ul PBS containing 50% Matrigel (Corning). After injection, the incision and the skin were closed with absorbable sutures. Four weeks after injection, the mice were euthanized and lungs were removed for use in subsequent experiments. For cotransplantation models, cancer-associated fibroblasts (CAFs) sorted as $CD45^-CD31^-EpCAM^-PDPN^+MHCII^+$ or $MHCII^-$CAFs from mouse orthotopic LLC tumor. $MHCII^+$ or $MHCII^-$ CAFs were combined with LLC tumor cells in a 10:1 ratio (5,000,000 CAFs/500,000 cancer cells, resuspended in 100ul PBS containing 50% Matrigel) and injected subcutaneously (s.c.) into C57BL/6J mice. Tumor volumes were monitored periodically using calipers from Day 7 and were calculated by applying the formula: (length x $width^2$)/2. For *in vivo* anti-PD-1 treatment, anti-PD-1 or PBS were administered intraperitoneally (i.p.) at a dose 200ug per mouse on day 7, 10, 13, 16 in cotransplantation mice (tumor cells were injected on Day 0). For anti-PD-L2, anti-RGMB, the dosage every time was 100ug. For mice in the control group, rat IgG2b isotype control or rat IgG2a isotype control were used as indicated. 21 days after LLC and CAFs co-injection, tumors were harvested for flow cytometry and immunofluorescence staining.

ELISA

Cell culture supernatants were harvested, concentrated and used for enzyme-linked immunosorbent assay (ELISA) kit (Servicebio, Wuhan, China). PDTF were cultured *ex vivo* for 24hrs to collect supernatants for ELISA measurements of IFNs. All experiments were performed according to the manufacturer's instructions.

Patient-derived CAFs 3D culture

All human NSCLC samples involved in this study were obtained with approval from the Ethics Committee of Shanghai Chest Hospital. Cancer and para-cancer tissues were collected from patients with NSCLC who underwent pathological biopsy or surgical resection at the Shanghai Chest Hospital with permission from the patients. All experimental procedures commenced within 30 min of sample collection. To improve the success rate of CAF cells isolation and culture, we employed two methods. Briefly, samples were mechanically minced into 1–2 mm^3 fragments with sterile disposable scalpels. A portion of the tissues were placed in 6-well uncoated culture plates with DMEM supplemented with 10% FBS to allow for CAF cells to grow out from tissues and expand until cells became confluent before passaging. The remaining tissues were dissociated using human Tumor Dissociated Kit (Miltenyi Biotec) with the gentleMACS instrument according to the manufacture's procedures. After digestion, the suspension was filtered through a 70μm sterile cell strainer (Miltenyi Biotec) to collect a single-cell suspension. The filtrate was centrifuged at 2000 rpm for 5 min. The cell pellet was resuspended with 1mL DMEM supplemented with 10% FBS and plated on 6-well uncoated culture plates. The non-adherent cells were removed after culturing for 1 h at 37°C to acquire purer CAF cells, because the adhesion time of fibroblasts was much shorter than tumor cells. The purity of fibroblasts was evaluated with WB and RT-qPCR. Primary CAFs were positive for FAP and α-SMA and negative for EpCAM, CD45 and CD31. After quality control and stabilization during passage 0 (the first 10 cm dish after dissociation from tumor tissue), CAFs were encapsulated in a GelMA-PEO phase-separation hydrogel (GelMA: 5 g/L; PEO: 0.1 g/L). PEO was washed away three times with sterile PBS. As established in our previous manuscript,[20] GelMA-PEO is non-immunogenic, which is crucial for co-culturing CAFs with autologous $CD4^+$ T cells to prevent non-specific immune activation. Following the removal of PEO, CAFs remained in GelMA (5,000 cells/10 μL) and were cultured in the same medium used for 2D settings. Each passage was defined by reaching a cell concentration of 50,000 cells/10 μL GelMA. GelMA was dissociated by treating with 0.1 mg/mL collagenase I for 5 min at 37°C. CAFs were used in subsequent experiments within 4 passages.

RNA sequencing for patient-derived CAFs

Patient-derived primary CAF cell-lines were extracted, passaged, and maintained as previously described. For this investigation, only CAF cell-lines within passage 4 were used for downstream experiments, including co-culture with $CD4^+$ T cells, and molecular biology assays. To exclude environmental influences, bulk RNA sequencing was performed only on CAFs at passage 0 (RNA was extracted as soon as CAFs were sorted by FACS). Total RNA was extracted from 1 million CAFs following the manufacturer's protocol using the TRIzol reagent (Invitrogen). The purity and quantity of the RNA were measured with the NanoDrop 2000 spectrophotometer (Thermo Fisher Scientific). RNA integrity was assessed using the Agilent 2100 Bioanalyzer (Agilent Technologies). Subsequently, libraries were prepared using VAHTS Universal V6 RNA-seq Library Prep Kit according to the manufacturer's instructions. The libraries were sequenced on Illumina Novaseq 6000 platform, generating 150 bp paired-end reads. The law reads in fastq format were initially processed using fastp, where low-quality reads were removed to obtain the clean reads. The clean reads were mapped to the reference genome using HISAT2. FPKM of each gene was calculated and the read counts of each gene were obtained by HTSeq-count. PCA were performed using R (v4.4.1) to evaluate the biological duplication of samples. Clinical information of patients from whom CAFs were isolated was listed in Table S2.

Single-cell RNA sequencing

For single-cell sequencing, all cells freshly dissociated from patients' tumors were sequenced, without sorting through FACS. Fresh NSCLC lung tumor tissues were transferred in MACS Tissue Storage Solution (Miltenyi Biotec) and kept on ice. The tube was centrifuged at 50 g for 1 min at 4°C, followed by the addition of 2 mL preheated digestion solution (Miltenyi Biotec) after discarding the tissue storage buffer. The tubes containing the lung cancer tissue were incubated in a 37°C water bath, with gentle pipetting performed 3 times every 5 min. Enzymatic incubation time was about 45 min. Once the incubation was completed, 10% FBS was added, and the solution was filtered using a 40 μm cell strainer (Corning). The suspension was centrifuged at 300 g for 3 min at 4°C and the red blood cells were removed using ACK lysis buffer (Roche). The suspensions were centrifuged at 300 g for 3 min at 4°C, and the pellets were resuspended in PBS with 0.01% Bovine serum albumin (Sigma). The cells were then loaded into microfluidic chip of Chip A Single Cell Kit v2.1 (MobiDrop, Zhejiang, China) to generate droplets with MobiNova-100 (MobiDrop, Zhejiang, China). Each cell was involved into a drop containing gel bead linked with up to millions oligos (cell unique barcode). After encapsulation, the drops underwent light cut by MobiNovaSP-100 (MobiDrop, Zhejiang, China), allowing the oligos to diffuse into the reaction mix. The mRNAs were captured by cell barcodes with cDNA amplification in droplets. Following reverse transcription, the cDNAs with barcodes were further amplified and a library was constructed using the High Throughput Single-Cell 3′ Transcriptome Kit v2.1 (MobiDrop, Zhejiang, China) and the 3′ Dual Index Kit (MobiDrop, Zhejiang, China). The resulting libraries were sequenced on an Illumina NovaSeq 6000 System. The raw data (fastq format) from the single-cell 3′ transcriptome was pre-analyzed using MobiVision (version 3.0, MobiDrop). The reads were aligned to the Homo sapiens reference genome GRCh38. A filtered cell-gene matrix was obtained using MobiVision. For further analysis, low-quality cells were filtered out according to the specified methods of disclosure. The clinical information for patients undergoing single-cell RNA sequencing was listed in Table S1.

The cell count and sequencing quality metrics were presented in Tables S3 and S5, respectively.

DSP spatial sequencing

For DSP spatial-sequencing, at least 2 patients for each group (pre, post-Non-MPR, post-MPR), and at least 4 visions for each patient were adopted for sequencing. This technology allows us to gate SMA^+ cells in the specific regions we designated to perform bulk-RNA sequencing. Three criteria need to be met to define fibrotic "hotspots": 1) In a certain region, fraction of SMA^+ cells within all nucleated cells is over 70%; 2) it is not a tracheal structure determined by pathologists; 3) it is within NSCLC TME, instead of locating at the tumor border area. Formalin-fixed and paraffin-embedded (FFPE) tumor samples were preserved at the time of surgical. Serially sectioned FFPE sections (5 μm) from each tissue was stained for histological analysis of hematoxylin and eosin (HE) and used as a reference for regions of interest (ROIs) selection. For ROIs selection, slides were baked at 60°C for 1 h, deparaffinized, rehydrated, and antigen-retrieved in Tris-EDTA buffer at 100°C for 15 min. This was followed by digestion with proteinase K for 15 min at 37°C to expose RNA targets. The slides were then postfixed with polyformaldehyde at RT for 5 min, hybridized over night at 37°C with a UV-photocleavable barcode-conjugated RNA *in situ* hybridization probe set. After hybridization, the slides were washed to remove off-target probes and counterstained with morphology markers at RT for 1 h in the dark. For DSP morphological labeling to select ROIs for three single-cell ROIs, the slides were labeled using fluorescently antibodies for total immune cells (anti-CD45, Nanostring), epithelial cell marker (anti-panCK, Nanostring), and fibroblasts (anti-αSMA, NBP2-34522AF647), along with syto13 (Nanostring). Immunofluorescence images, ROIs selection, segmentation into marker specific areas of interest (AOIs), and spatially indexed barcode cleavage and collection were performed on a GeoMx DSP instrument (Nanostring). A total of 35 ROIs were collected for 6 NSCLC tumor samples (2 naive, 2 MPR, 2 non-MPR), followed by UV light to cleave the probe tags (oligo) within the selected ROIs. The cleaved oligos were collected into a 96-well plate via capillary action and then transferred to a PCR plate for library preparation and sequencing. Each well of the PCR plate contained primers with specific barcodes, adding a unique library tag to each ROI. The prepared libraries were subjected to high-throughput paired-end sequencing using the Illumina sequencing platform. In Read 1, the sequences included a 14 bp unique molecular identifier (UMI) for quantifying expression levels; in Read 2, the sequences included probe tag fragments for aligning the probe library to determine the corresponding genes. The clinical information for patients undergoing DSP-spatial sequencing was presented in Table S1.

Single-cell data analysis

Cell Ranger Single-Cell toolkit (version 6.1.2) was applied to align reads against the GRCh38 human reference genome and generate the preliminary unique molecular identifier (UMI) matrix. The R package Seurat (version 4.4.1) was used to analyze the scRNA-seq data. We performed stringent quality control from Prof. Zhang[56] to filter out low-quality cells. Cells with (1) less than 600 or more than 25,000 UMI counts, (2) less than 600 detected genes, or (3) more than 5% mitochondrial genecounts, (4) doublets (calculated using DoubletFinder (version 2.0.4). In each sample, the threshold for determining whether a cell is doublets is calculated by multiplying the cell count by 5*1e−6.), (5) ambient RNA if below 0.2 (calculated using decontX (version 1.4.0)) were filtered out. We then adopted the Seurat-implemented NormalizeData function to perform the library-size correction and logarithm transformation, with the obtained expression matrix used for downstream analyses.

We then adapted the workflow of Seurat to perform dimension reduction and unsupervised clustering. First, the top 2000 highly variable genes (HVGs) were selected by the FindVariableFeatures function (Seurat) with the parameter selection.method = "vst". Effects of the total UMI count and mitochondrial gene percentage were then regressed out from the HVG expression matrix with the ScaleData function (Seurat). The principal component analysis was then performed by the RunPCA function (Seurat) on the scaled

HVG expression matrix, retaining the top 50 components for downstream analyses. Because the single-cell library was constructed for each patient at each treatment time point separately, we regarded the combination of patient and treatment point as the batch indicator and removed the batch effect from different experiments with the harmony algorithm. In the batch-corrected space, UMAP implemented by the RunUMAP function (Seurat) was adopted for dimension reduction, with the resulting cell embedding coordinates used for visualization. The harmony components was selected as dimensional reduction technique to use in construction of Shared Nearest-Neighbor (SNN) graph. We systematically performed a two-round unsupervised clustering based on the FindClusters function (Seurat) to uncover the cellular population structure with the resolution 0.1 and 0.2. During the first round of clustering, we annotated each cluster by the expression of canonical cellular makers, including CD3E, CD4, CD8A, EPCAM, COL1A1, FCGR2A, PECAM, IGKC, MS4A1, TPSAB1 (Figure S1C). Then for $CD4^+$T cells, $CD8^+$T cells and CAF, we performed a second round of unsupervised clustering to identify fine-grained cell subtypes with the above-described procedure but only on the expression matrix of cells from the analyzed major cell type, and further defined them with references to literatures. The proportion of each fine-grained cell subtypes relative to the major cell type in each patient will be used for subsequent subcluster change analysis.

For In-house supplementary dataset (14 samples), we used In-house discovery dataset (10 samples) as reference UMAP structure to query a projection. This was achieved by calling the FindTransferAnchors and MapQuery function[57] (Seurat V5). The gene markers for the annotation of CAFs subtypes was listed in Table S4.

Deconvolution based on GEPIA2021

In Figures 4D, 5D, and 7D, the expression of PDCD1, PDCD1LG2, and CD279 was analyzed in a cell-subcluster-specific manner using TCGA bulk RNA sequencing datasets (TCGA-LUAD, TCGA-LUSC). The boxplots were generated at http://gepia2021.cancer-pku.cn/sub-expression.html. Li et al. established cell type-level differential expression through a deconvolution method and reference mapping based on single-cell data.[58] The in-browser ANOVA module was used to perform the analysis.

Publicly-available bulk-RNA sequencing datasets analysis

In Figures 3O, 4E, 4H, 7B, and 7C, publicly available datasets were re-analyzed, specifically GEO: GSE253540, GEO: GSE211044, and GEO: GSE121251, using R. If the bulk RNA expression data in these datasets were already normalized, they were directly used for downstream analysis. For original count data, batch effects across different datasets and samples were removed using the *removeBatchEffect* function in the R package *limma* before downstream analysis. GEO: GSE253540 contains bulk RNA sequencing data of conventional $CD4^+$ T cells (Tconv) and Tregs from various human donors, stimulated *ex vivo* with anti-TNFR2 and anti-CD28 before sequencing. During our re-analysis, samples were regrouped into Tregs or Tconv, with effects from different treatments regressed out, followed by DEGs analysis. GEO: GSE211044 comprises bulk RNA-seq data of different immune cell subtypes (including Tconv, Tregs, and $CD8^+$ T cells) sorted from the PBMC/TME of healthy donors or NSCLC patients without *ex vivo* stimulation. In our manuscript, GEO: GSE211044 is considered as *in vivo* data and GEO: GSE253540 as *ex vivo* data. GEO: GSE121251 includes FOXP1 KO Tregs sorted from mice PBMC ($FOXP3^{Cre-FOXP1-/-}$), with control Tregs sorted from $FOXP3^{Cre-FOXP1-fl/fl}$ mice. Activated Tregs (aTregs) refer to Tregs stimulated *ex vivo* with anti-CD3/28.

Public spatial transcriptomics analysis

GEO: GSM5420749, GSM5420750, GSE181300, and CRC_10X datasets visualization was conducted at: https://www.spatialtme.yelab.site/#!/browse. The featureplots of specific cell-type signature genes expression were produced by the ''analysis'' module online.[59] The signature genes of apCAFs and $FOXP1^+$Tregs were the average expression of the top 20 marker genes of their corresponding cell-subsets in our own single-cell dataset, calculated by *AddModuleScore* and *FindAllMarkers* function in the R package *Seurat*.

Biobank of patients TME

3D culture of patient-derived organoids or CAFs in gelatin methacryloyl (GelMA)–poly (ethylene oxide) (PEO) based hydrogel was accomplished as previously described.[20] GelMA-PEO phase-separation hydrogel was proved by us before to have the non-immunogenicity nature, making it compatible for co-culture of immune cells and tumor cells. We first separate the tumor specimens from one patient into three equal parts (A, B, C) at day0. For A, we generate organoids from it in Matrigel as previously-described. For B, we dissociate it and sorted TILs out (CD45 (TIL) Microbeads, human, cat: Miltenyi 130-118-780), then used the anti-CD28/CD3 beads (Dynabeads Human T-Activator CD3/CD28, cat: 11161D) to expand them into at least 3×10^6 cells and cryopreserved them, used within 1 month. For C, we applicated it to get the CAF cell-line, and the CAF cell-line was constructed as described in the method ''patient-derived CAF 3D culture''. At day28, we used mechanic dissociation (without any enzymes) to extract organoids, and accutase (StemCell: 07920) to extract CAFs, and recovered TILs. We FACS-sorted them respectively (organoids: $CD45^-EPCAM^+$; TILs: $CD45^+EPCAM^-$; CAFs: $CD45^-EPCAM^-CD31^-$) then performed RT-qPCR upon them respectively.

Construction of PDTF platform

PDTF platform was established as previously described.[28] Tumor fragments from biopsy or surgery of patients undergoing NCIT were collected immediately within 2 h after surgery for subsequent PDTF cultures. They were manual cut into small tumor pieces of 1–2 mm^3 size on ice. After processing, all PDTFs were cryopreserved in liquid nitrogen until further usage. For a specific

patient, we performed downstream analyses such as mFC until we had got his/her post-treatment tumor samples, together with pre-treatment samples recovered from liquid nitrogen preservation, to avoid batch effects. To prevent lymphocyte efflux, individual PDTFs were embedded in the same hydrogel we used for patient-derived CAF 3D culture. One PDTF per well was placed on top of the GelMA-PEO matrix, after which a second layer of 40-μL matrix was added. Where indicated, tumor medium was supplemented with anti-PD-1 antibody (nivolumab; Bristol Myers Squibb) at 20 μg/mL final concentration. Control cultures were carried out in the presence of control human anti-β-Gal-hIgG4 (S228P; InvivoGen) at 10 μg/mL. Eight to ten PDTFs were used per condition. Unless indicated otherwise, PDTF cultures were kept at 37°C for 48 h before readout.

Co-culture of $CD4^+$ T cells with CAFs

The co-culture of $CD4^+$ T cells with autologous primary CAF cell-line from the same patient was accomplished as previously-described.[27] Naive $CD4^+$ T cells were sorted from PBMC (MojoSort Human CD4 Naive T cell Isolation Kit, com: Biolegend, cat: 480042) and then cultured in the following medium setting for 24hrs: 25ul/ml anti-CD3/28 (ImmunoCult Human CD3/CD28 T cell Activator, com: StemCell, cat: 10971), 400 ng/ml human IL-2 (Peprotech, cat: 200-02), 4 ng/ml human TGF-β (Peprotech: 100-21), 200 nM/ml retinoic acid (MedChemExpress, cat: HY-14649), RPMI 1640 Medium (Thermo, cat: 11875093), 10%FBS (Gibco, cat: 10099141), 1%Penicillin-Streptomycin (Thermo, cat: 15140122). CAFs from the same patient was dissociated from 3D culture settings using accutase as described aforementioned, and then sorted to apCAFs ($PDPN^+HLA\text{-}DR^+$) or non-apCAFs ($PDPN^+HLA\text{-}DR^-$). apCAFs or non-apCAFs were co-cultured with autologous naive $CD4^+$ T cells (after incubation for 24hrs) at the ratio of 1:20, for 48hrs, with the supplement of 200 nM/ml rapamycin (MedChemExpress, cat: 53123-88-9). As indicated, medium was supplemented with anti-PD-1 antibody (nivolumab; Bristol Myers Squibb) at 20 μg/mL final concentration before mFC or FACS profiling. For murine $CD8^+$ T cells function profiling in Figure 4J, FOXP1high Tregs meant Tregs sorted from tumors of the "apCAFs+tumor+anti-PD1" group, and FOXP1low Tregs meant Tregs sorted from tumors of the "non-apCAFs+tumor+anti-PD1" group. The criteria for determination of high expression of FOXP1 was 10% of $CD4^+$ TILs. Tregs were sorted by FACS ($CD45^+CD4^+CD25^+$). FOXP1high Tregs or FOXP1low Tregs were co-cultured with $CD8^+$ T cells sorted from murine spleens using FACS at the ratio of 2:1. After 4hrs, the cell activation cocktail (Biolegend; No. 423303) was used to conduct stimulation for 6hrs (1:500), and then GZMB was profiled by mFC immediately.

QUANTIFICATION AND STATISTICAL ANALYSIS

The sample size, statistical methods, and relevant details are provided in the figure legends, main text, or methods section. Data were analyzed using R (version 4.3.1 or version 4.4.1). Results with $p < 0.05$ were considered statistically significant. Sample size estimation was based on assay sensitivity, expected heterogeneity, published literature, and pilot studies. Data are presented as means with either standard error of the mean (SEM) or standard deviation (SD), and error bars represent SEM or SD from at least three independent experiments. Statistical analyses included 2-tailed Student's t test, one-way ANOVA followed by Dunnett's tests, chi-square test, nonparametric Mann-Whitney U-test, and Kaplan-Meier survival analysis with log rank (Mantel-Cox) test, as appropriate. Detailed statistical information for each experiment is provided in the corresponding figure legends. $^{****}p < 0.0001$; $^{***}p < 0.001$; $^{**}p < 0.01$; $^{*}p < 0.05$; ns, no significance.